FISEVIER

Contents lists available at ScienceDirect

# Spectrochimica Acta Part B: Atomic Spectroscopy

journal homepage: www.elsevier.com/locate/sab





# Variably weathered ultramafic rocks: Investigation of their mineralogy with SuperCam-like techniques

C. Collet <sup>a</sup>, A. Cousin <sup>a</sup>, <sup>b</sup>, O. Beyssac <sup>b</sup>, P. Beck <sup>c</sup>, O. Forni <sup>a</sup>, S. Clegg <sup>d</sup>, J. Comellas <sup>e</sup>, E. Clavé <sup>f</sup>, A. Fau <sup>a</sup>, S. Pont <sup>b</sup>, F. Poulet <sup>g</sup>, R.K. Martinez <sup>d</sup>, H. Austrheim <sup>h</sup>, S. Maurice <sup>a</sup>, R.C. Wiens <sup>i</sup>

- a Institut de Recherche en Astrophysique et Planétologie, Université de Toulouse 3 Paul Sabatier, CNRS, CNES, Toulouse, France
- <sup>b</sup> Institut de Minéralogie, de Physique des Matériaux et de Cosmochimie, CNRS UMR 7590, Sorbonne Université, Muséum National d'Histoire Naturelle, Paris, France
- <sup>c</sup> Université Grenoble-Alpes, CNRS, IPAG, UMR 5274, Grenoble, France
- <sup>d</sup> Los Alamos National Laboratory, NM, USA
- e University of Hawai'i at Mānoa, USA
- f DLR, Berlin, Germany
- g Institut d'Astrophysique Spatiale, CNRS, Université Paris-Saclay, 91400 Orsay, France
- <sup>h</sup> The Njord Center, Department of Geology, University of Oslo, P.O. Box 1048, Blindern, Oslo, Norway
- i Purdue University, IN, USA

# ARTICLE INFO

# Keywords: Mars2020

SuperCam Serpentinization

# ABSTRACT

The NASA Perseverance rover is exploring Jezero crater on Mars since February 2021. Orbital data from Nili Fossae and Jezero crater show a wide diversity of mineralogical signatures including primary mineral like olivine as well as diverse secondary minerals like clays and serpentines and one of the strongest spectral signatures of carbonate on Mars from orbit. This olivine and carbonate-bearing unit is regionally extensive. Most of the studies interpreted the relationship between olivine and carbonate-bearing units as a result of weathering processes involving fluid-rock interactions such as serpentinization and carbonation. Since February 2021, Perseverance has confirmed this large diversity of primary and secondary minerals. The detection of serpentine is of particular interest in order to better constrain the past environment at Jezero crater. Among the science payload, SuperCam is combining three spectral techniques (Laser-Induced Breakdown Spectroscopy - LIBS, Raman, and Visible and near InfraRed - VISIR) that give access to the elemental composition of the targets but also to their mineral and molecular structure. Here, we use terrestrial ultramafic rocks with various degrees of alteration that were well characterized from previous studies, and we analyze them with SuperCam replicate laboratory setups to investigate the sensitivity of SuperCam to detect olivine and secondary phases, in particular serpentines. Distinguishing serpentine from olivine by LIBS is challenging since they have similar chemistry. On the other hand, Raman spectroscopy is able to detect all the phases present in the analyzed samples, when their content is high enough. Finally, the VISIR technique detected the secondary phases while it did not observe easily the olivine. We found that the synergy between these three techniques is of particular importance to differentiate such specific phases, which occur as intricate mixtures down to the sub-micrometer scale in natural targets.

# 1. Introduction

Perseverance landed in Jezero crater, located in the Nili Fossae region, Mars, on February 18th, 2021. The goal of this mission is to identify samples of astrobiological interest and characterize their environment at the surface of Mars [1]. Some of these samples are collected and are planned to be returned to Earth in the future by the NASA/ESA Mars Sample Return Program (MSR). Jezero crater is a 45

km wide ancient lake system, estimated to be older than 3.5 billion years. It locally hosts a well preserved delta fan deposit presenting some diverse mineralogies, including clays and carbonates from orbital signatures [2]. Orbital data from Nili Fossae and Jezero crater show a wide diversity of mineralogical signatures including olivine and pyroxene as well as clays, serpentines and one of the strongest spectral signatures of carbonate on Mars from orbit. This olivine and carbonate-bearing unit

E-mail address: agnes.cousin@irap.omp.eu (A. Cousin).

<sup>\*</sup> Corresponding author.

is regionally extensive [3,4,4–10]. In general, these studies interpreted the relationship between the olivine and the secondary minerals as a result of aqueous alteration processes involving serpentinization and carbonation [9,11,12].

Among the science payload onboard Perseverance, SuperCam is a multi-technique instrument performing remote analysis of the targets. It is being used to analyze rocks and soils with its five subsystems [13,14]. The Laser Induced Breakdown Spectroscopy (LIBS) can determine the elemental composition of the targets, while Raman and VISIR [15] spectroscopy give access to their mineral and molecular structure. In addition, SuperCam includes a color Remote Micro Imager (RMI) which provides context imagery for each SuperCam analysis of the targets. The fifth technique consists in a microphone that provides information about the atmospheric processes like wind or turbulence, and gives also access to some physical parameters of the rock targets analyzed by LIBS.

Olivine and pyroxene spectral signatures were detected from orbit in Jerero crater's floor [2-5], of prime importance for understanding the magmatic activity of the planet, its evolution, and a better refinement of the crater chronology via the sampling. Perseverance has confirmed in situ orbital detections of olivine and pyroxene in the crater floor, and has revealed that the two main formations Séitah and Maàz are igneous and not sedimentary [16-20]. Perseverance has shown that these igneous rocks are relatively pristine [19,20], with only a few local secondary phases due to fluid-rock interactions such as clays, sulfates, perchlorates and/or carbonates [17,21-23]. These secondary minerals are sometimes associated with serpentine and/or carbonates in Séitah rocks, as seen from the PIXL data [23]. No serpentine has been detected by SuperCam in these rocks, probably due to their very fine scale. In Màaz, SuperCam has not detected any serpentine either, but the association of the PIXL scans and the SuperCam VISIR data may help identify some Fe-rich serpentines [24,25], even though serpentine is not always easily differentiated from other phyllosilicates [26,27]. The delta front of Jezero crater has shown to be much more enriched in secondary phases (Fe/Mg-rich phyllosilicates, Fe-Mg carbonates, sulfates and even serpentines locally), revealing either different sediment sources or different alteration or diagenetic processes [28,29]. Nevertheless, the serpentine that has been detected is very local, and detected by VISIR only. The LIBS data support this detection but are not sufficient on their own to identify the serpentine in this specific outcrop. More recently, the Margin Unit [30] revealed the strongest content of Fe-Mg carbonates [31], but SuperCam did not find any no evidence for serpentine signatures. Some PIXL data, after correction from the S and C content, could have detected a few points enriched in Fe-rich serpentine [32]. The first results from the transition between the margin unit and the crater rim [33] do not show either any strong serpentine detection from all instruments [34-37]. The SuperCam VISIR technique shows some detection of some Mg-rich clays, but without any strong characteristics to conclude on the mineralogy [34].

Fluid–rock interactions may significantly alter ultramafic rocks involving various reactions such as serpentinization. This alteration may modify significantly the rocks' bulk physical properties and possibly their chemistry. Among various reaction pathways, an example of a classical equation for serpentinization occurring during hydrothermalism in a temperature ranging from ambient to about 400 °C [38] is:

$$2Mg_2SiO_4 + 3H_2O \rightarrow Mg_3Si_2O_5(OH)_4 + Mg(OH)_2$$
  
That is

 $forsterite + water \rightarrow serpentine + brucite$ 

Serpentinization is one among various chemical reactions occurring during such alteration processes, which can generate various mineral phases like carbonate, serpentine and talc.

The stoichiometric equivalences obtained from the chemical formula are:

```
olivine: (Mg, Fe)_2[SiO_4] \rightarrow (Fe + Mg)/Si = 2
```

serpentine:  $(Mg, Fe)_6Si_4O_{10}(OH)_8 \rightarrow (Fe + Mg)/Si = 1.5$ 

On Earth, serpentine is rarely found as a pure mineral phase and is rather often mixed with primary minerals as well as other alteration phases. When the serpentinization process is not complete, serpentine phases are often found in replacement textures (e.g., mesh texture) or within fractures inside other minerals. If the process is further advanced, serpentine phases will become more abundant, but serpentine will rarely appear as pure since other mineral phases are formed during the alteration process. Identifying serpentines, but also other alteration phases, is a challenge since these phases are intimately mixed down to the sub-micrometric scale, even on Earth [39]. In this article, we investigate in laboratory various ultramafic rocks from Norway that were variably altered by fluid–rock interactions and that are well characterized [40–42].

The objective of this study is to investigate the possibility of detecting serpentine and other alteration phases and distinguishing them from the primary mineralogy (e.g. olivine) by using experimental setups which are replicates of the SuperCam instrument. The expected outcome is to determine a strategy to improve the chemical and mineralogical characterization of such complex rock in situ on Mars using the SuperCam instrument suite.

# 2. Sample description

The two rocks analyzed for this study are variably serpentinized ultramafic rocks from Norway. These rocks are particularly interesting since their petrology and geochemistry have been exhaustively characterized and the protolith as well as the alteration processes have been investigated in detail. Here, we use these rocks as possible analogues to the variably altered rocks of the Nili fossae region detected from orbit and locally investigated by Perseverance.

Notably, the protoliths of these samples (igneous olivine-rich rocks) bear some similarity in terms of primary composition with the rocks observed in the Séitah formation [20] as well as in the Margin units [21]. These samples have undergone multiple cycles of alteration. One of these cycles includes serpentinization in a low-temperature hydrothermal environment. Subsequently, these rocks were also altered by meteoritic waters. Such context for alteration is plausible for Mars in the past.

The first sample named ROR0311 comes from an altered ultramafic body originating from Feragen in Norway [42]. The protolith rock is an alpine peridotite, a dunite, and it was in situ altered for a long period with likely several weathering stages including current alteration under arctic conditions. The sample used for this study covers the three textural zones (Fig. 1a) described by [41,42] with a fresh core showing a typical mesh texture made of serpentine and brucite enclosing relicts of primary olivine with minor chromites. In the weathered rinds (called hereafter "alteration 1" and "alteration 2"), brucite disappears and is replaced by pyroaurite, and carbonates are detected mostly in veins.

The second sample named Solund, originates from the Solund region in Norway [40]. This sample consists of an altered peridotite boulder from a conglomerate collected in a Devonian basin. Again, the rock has undergone a long and polyphased alteration history that resulted in spectacular color zoning in the boulder section. In our sample (Fig. 1b), the greenish core of the rock is more serpentinized compared to ROR0311 as it shows a mesh texture where the relict olivine is fully replaced by serpentine, a Deweylite assemblage and minor carbonates. The dark rim zones (called "alteration 1") consist of talc with variable amounts of carbonates while the external reddish rim (called "alteration 2") is dominated by talc and hematite with the presence of carbonates. At the outcrop scale, various degrees of serpentinization for the protolith (core) are observed and various degrees of weathering have been described, the ultimate one consisting in an hematite-stained calcite and quartz-rich assemblage, nearly a jasper. Further details on these rocks can be found in [40-42].

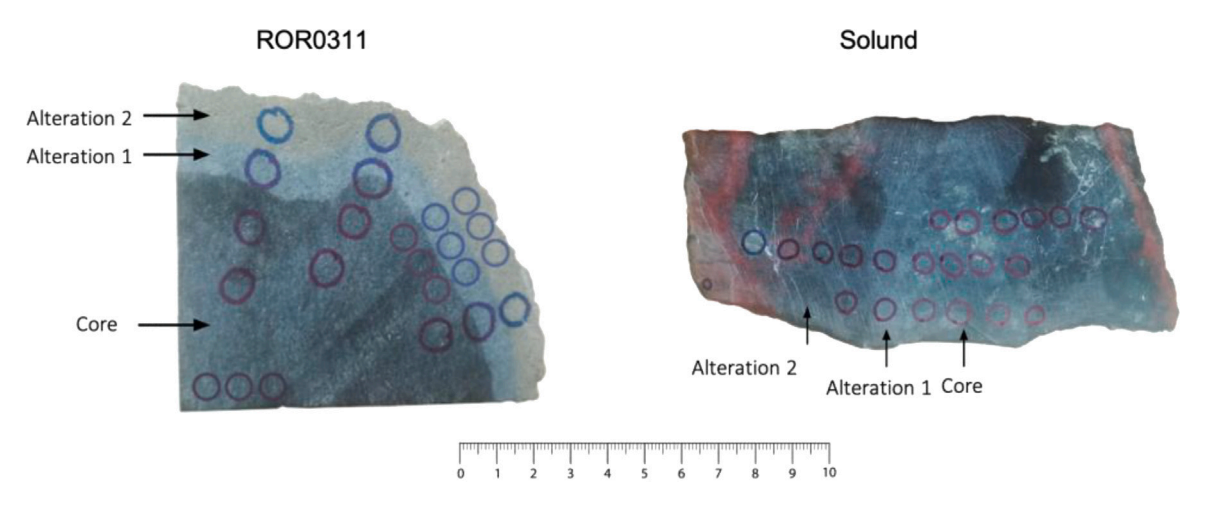


Fig. 1. (Left) Photograph of the rock section of sample ROR0311 from Feragen (Norway). The three alteration zones are well identified: the core in dark grey, the alteration 1 in light gray and the alteration 2 in yellow-ish. (Right) Photograph of the rock section from Solund (Norway). The three alteration zones are discernable: the core in grey, the alteration 1 in light gray and the alteration 2 in dark gray with red zones. The scale is shown for both targets (ROR0311 is about 10 cm wide and Solund is about 13 cm wide). The circles in both samples represent the areas analyzed with LIBS (See supplementary material for more details, Figures S24 and S25).

# 3. Methodology

The two samples were cut from the rock in two halves (Fig. 1) with a diamond saw. The first half with a raw surface from the cut was used for SuperCam-like techniques: LIBS, time-resolved Raman and VISIR spectroscopy. From the second half of the rock, polished petrological thin sections were prepared for analysis with Raman microspectroscopy and Scanning Electron Microprobe (SEM).

# 3.1. Raman: SuperCam-like and micro-Raman

The polished thin sections were analyzed using a continuous-wave (CW) Raman microspectrometer Renishaw InVia Reflex for point analyses and Raman hyperspectral mapping. All measurements were performed using a green 532 nm solid-state laser focused on the sample through a Leica DM2500 microscope with a short-working distance 50X objective (NA = 0.75). This configuration yielded a horizontal resolution of  $\approx$  1–2  $\mu m$  for a laser power delivered at the sample surface set at less than 1 mW using neutral density filters to prevent irreversible thermal damage. This corresponds to a laser irradiance in the range of 0.3-1.3.109 W m<sup>-2</sup> [43]. All point measurements were performed with a circularly polarized laser using a 1/4-wave plate placed before the microscope in order to minimize polarization effects. The Raman signal was dispersed by a grating with 2400 lines/mm and the signal was analyzed with a RENCAM CCD detector. For Raman mapping and the acquisition of hyperspectral maps, the sample was moved with an appropriate step size using a XYZ Renishaw motorized stage. Laser focus was optimized by correcting topographic variation prior to analysis (surface mode using the Renishaw Wire 4.3 software), and all maps were processed using the Wire 4.3 software. To process the hyperspectral maps and build the mineralogical composition maps, we used an algorithm provided by the Renishaw software and based on DCLS (Deep Constrained Least Square) deconvolution, using reference spectra for each mineral phase. The analysis gives a map with a color code to highlight each mineral phase and is described in [44]. All measurements were performed at controlled room temperature.

The distribution of the mineralogical phases highlighted in the map has been calculated using the software Gimp. The methodology used was to count the pixels associated with a color (linked to a mineral). Knowing the total number of pixels in each map, it was therefore possible to obtain the percentage of the presence of this mineral in the image. This micro-Raman mapping provided semi-quantification across the mapped areas as presented in Figs. 2, 3, 10 and 11.

The raw cut surfaces of each sample were also analyzed using a custom time-resolved (TR) Raman and luminescence spectrometer described by previous studies [43,45-47]. This instrument includes a Raman microscope (micro TR Raman) as well as a telescope (remote TR Raman) in a configuration similar to the SuperCam instrument. The laser is a nanosecond (1.2 ns FWHM, 1mJ per pulse) pulsed Diode-Pumped Solid State laser operating at 532 nm with a 10 to 2000 Hz repetition rate. Here, we used the remote configuration: the laser is collimated at the sample surface 8 m from the telescope Schmidt plate on a spot of  $\approx$  6 mm diameter, and the Raman signal is collected by a conventional Schmidt-Cassegrain telescope (Celestron-C8 202 mm diameter Schmidt plate) on a spot of  $\approx 5$  mm diameter co-aligned with the laser spot. The laser is linearly polarized in the remote TR Raman as for SuperCam and the possible polarization effects on the relative intensity of the Raman peaks are not investigated here. A Notch filter cuts off the Rayleigh scattering at  $\approx 90~\text{cm}^{-1}$  and the signal is collected by an optical fiber and sent into a modified Czerny-Turner spectrometer (Princeton IsoPlane 320) coupled with an intensified Princeton PIMAX4 ICCD camera. The fine control of both time delay and gating time of the camera allows sub-nanosecond time resolution experiments thanks to an accurate synchronization between the laser pulse and the ICCD. This spectrometer has three motorized gratings which can be selected depending on the spectral window and resolution requested for the experiment. Here we used a grating with 600 lines/mm providing a spectral resolution of 10-12 cm<sup>-1</sup> similar to that obtained with SuperCam Raman. Irradiance associated with a pulsed laser can be roughly estimated as  $Q/(\tau S)$ , with Q = P/f being the laser energy per pulse, P being the time-integrated laser power measured at the surface of the sample, f the laser repetition rate,  $\tau$  the pulse duration, and S the surface of the laser spot on the sample [43]. Irradiance was set at  $\approx 10^{10}~\text{W}~\text{m}^{-2}$  which is conservative even in the case of absorbing minerals [43]. In remote TR Raman we use a 100 ns ICCD gate similar to that used with SuperCam and centered on the laser pulse (1.2 ns pulse for the laboratory instrument versus 4 ns for SuperCam). For this study, 200 000 to 500 000 laser shots have been used for each point analysis.

Calculating the Fo# (corresponding to the elemental ratio of Mg/(Fe+Mg)) of the olivine using the Raman spectra can be very useful to better understand the nature of the olivine and its conditions of formation. The Fo# has been calculated using the technique described in [48]. The technique consists in using the two characteristic peaks of olivine (DB1 and DB2) in the Raman spectrum, positioned at 823 and 855 cm<sup>-1</sup> approximately, and compute the olivine Fo#, by using the

DB2 equation provided by [48]. This has been applied to SuperCam Mars data in different papers [20,21].

# 3.2. LIBS

In this study, the LIBS analyses were performed using the SuperCam replica at two locations: at IRAP (Toulouse, France), and at Los Alamos National Laboratory (LANL, USA) which is calibrated to get quantitative chemical data. The SuperCam LIBS technique (for all SuperCam replica) uses a Nd:YAG crystal laser, with an emission at 1064 nm, and an irradiance exceeding 10 MW mm<sup>-2</sup>. SuperCam is also equipped with three spectrometers covering from the UV to the near Infra-Red range (UV:243.7-345.0 nm, VIO: 379.0-465.0 nm, Tspec: 532-853 nm - [13,14]). The Tspec (Transmission Spectrometer) corresponds to one spectrometer that covers three bands: Green (535-620 nm), Orange (620-712 nm) and Red (712-853 nm) [13]. The samples were placed at around 3 m from the instrument, in a martian chamber replicating the Mars atmospheric composition and pressure (Figure S19). At this distance the analytical footprint of LIBS is around 220 µm [14]. We tried to acquire the spectra from the same spot on the rock between the two setups. However, it is possible to have a few um difference in position between the IRAP and the LANL points.

The IRAP setup is made of the Engineering and Quantification Model for the Mast Unit (MU-EQM) and of the Engineering Development Unit model for the Body Unit (BU-EDU). At LANL, the SuperCam setup is composed of the refurbished first version of the flight model for the Mast Unit (MU-FM1) and of the BU-EQM. Both setups are overall similar, and similar to the SuperCam FM (BU and MU). More information can be found in Wiens et al. [13] for the Body Unit and Maurice et al. [14] for the Mast Unit. These models have nevertheless some specific characteristics: the LANL setup is used under cold temperature ( $\approx$ 0 °C) in order to have an optimum laser energy; while the IRAP setup, for its part, does not need to be cooled down, except the spectrometers that must be cooled to 15 °C for a better signal to noise ratio.

Quantitative elemental-calibration models are developed using a spectral database of 334 standards analyzed with the LANL setup, enabling the SuperCam team to extract quantitative chemistry from Mars data [49]. Only major elements are quantified for now (Si, Ti, Al, Fe, Ca, Na, K), whereas for minor and trace elements the effort is still ongoing [50]. The estimated accuracy of the major-element quantifications are around 6.1 wt% (SiO<sub>2</sub>), 0.3 wt% (TiO<sub>2</sub>), 1.8 wt % (Al<sub>2</sub>O<sub>3</sub>), 3.1 wt% (FeOT), 1.1 wt% (MgO), 1.3 wt% (CaO), 0.5 wt% (Na<sub>2</sub>O), 0.6 wt% (K<sub>2</sub>O), although a better estimate is given as a function of predicted composition [49]. The precision is significantly better than the accuracy, enabling the SuperCam LIBS data to be used to distinguish trends in composition and the possibility of doing some stoichiometric analysis [17,19,20,49].

LIBS spectra can also be used directly in a qualitative way, comparing some peak areas or ratios. Elemental peak areas can however follow a different trend than the quantitative content of the same element, as only one elemental peak is used for the qualitative investigation, whereas the quantitative models use the entirety of the spectral range (and therefore a multitude of peaks for this specific element - [49]). Moreover, the qualitative observations are not necessarily linear with their quantitative information due to several factors such as the matrix effects [51]. Nevertheless, it is generally assumed that the higher the peak area, the higher the quantity of the associated element. Several elemental lines of interest have been fitted in order to retrieve their peak areas. The fits were performed using a Lorentzian function. The fitting algorithm employed the Levenberg-Marquardt technique [52] to solve the least-squares problem and to optimize the adjustment of Lorentz parameters to the data points. For this study, elements of interest are Fe, Mg and Si, as they are part of the crystallographic structure of olivine and serpentine minerals. Hydrogen signal is also of interest to trace the presence of serpentine. Finally, the C line has

**Table 1**Principal elements analyzed with LIBS and the position of their peaks of interest in the spectrum.

Mg II	448.24 nm
Si II	634.9 nm
Fe I	438.48 nm
CI	658 nm
ΗI	656.5 nm

been investigated as well, as some carbonates are significantly present in the Solund sample. All the elements of interest for this study have several emission lines, and the selected ones are listed in Table 1. This selection was based on results from [53]. Before the fitting process, spectra are normalized to the total intensity of the spectral range of interest (UV, VIO, Green, Orange, Red) in order to correct for any bias related to the ablated volume, and therefore better compare spectra acquired from different targets and/or different setups. Concerning the H and C signals, they are normalized to the Oxygen triplet at  $\approx 778$  nm, as described in [21,54,55].

In this study, the H/O and C/O ratio are useful to investigate any possible the trend from the core to the alteration 2 of both targets. Nevertheless, their absolute values between the two different setups do not seem directly comparable. Indeed, a very slightly different gas is used to mimic the Mars atmosphere in the two laboratories. In Toulouse a mixture as close as possible as the Mars atmospheric composition (1.7% Ar, 2.6% N, 95.7% CO<sub>2</sub>) is used, whereas at LANL a pure CO<sub>2</sub> gas is injected into the chamber. Moreover, the pressure in the Mars chamber is slightly higher at LANL compared to IRAP (7.3 mbar vs 7 mbar, respectively). These very minor differences do not have any impact for most of the elements, but could possibly be relevant when looking at the signal from C and O, as most of it comes from the atmospheric contribution as shown in [55]. Concerning the H signal, it is highly dependent on the relative humidity, as samples can have some adsorbed water on their surface. In our study no specific approach to handle the samples has been applied to investigate the H signal in a quantitative way, and therefore they have not been heated nor maintained with Silica gel to avoid any adsorption of humidity. In such case, H/O signal can be used to investigate the trend between the different areas of the rock, for each setup, but the absolute values cannot be compared between the two setups, as the humidity is different between IRAP and LANL.

# 3.3. VISIR

The SuperCam infrared spectrometer [15] is an opto-acoustic filter based instrument, providing reflectance spectra in 1.3–2.6  $\mu m$  spectral range. The instrument spectral resolution is 32 cm $^{-1}$  (5 nm at 1.3  $\mu m$  and 21 nm at 2.6  $\mu m$ ) and provides reflectance spectra with Signal to Noise Ratio (SNR) typically > 50 [27,56]. The IR reflectance observation can be completed by using the LIBS spectrometer in passive mode to collect the visible part of the spectra between 400 and 850 nm [27, 57].

In order to provide IR spectra comparable to SuperCam IRS, we used the Shadows instrument [58] installed at IPAG (Grenoble, France). This monochromator-based system uses a synchronous detection technique to measure reflectance spectra up to 5  $\mu m$ . This setup has an approximately 5.2 mm diameter beam size, comparable to SuperCam footprint for targets at 4.5 m from the rover. The spectra were obtained with a 10 nm spectral sampling at a roughly 20 nm spectral resolution. Spectra were measured using a combination of Si (wavelength < 1000 nm) and InSb detectors (wavelength > 1000 nm).

## 3.4. Scanning electron microscope

We used Scanning Electron Microscope (SEM) to characterize the elemental chemistry of the two rocks in various zones by Energy Dispersive X-ray (EDX) spectroscopy in mapping mode to compare with elemental chemistry retrieved by LIBS. It is important to precise that SEM-EDX mapping was done on polished thin sections while LIBS analysis was done on the rock slab, so there is no direct correspondence between the areas analyzed (see supplementary material for more details, Figures S20 and S21). We used the TESCAN CLARA (FEG-ESEM/dual-EDS) SEM of the Electron Microscopy and Microanalyses Technical Platform of the Museum National d'Histoire Naturelle (Paris, France). To preserve some area of the thin section from carbon coating for other analysis (e.g., Raman spectroscopy), a part of each thin section was covered by aluminum foil during the coating process which deposited a 15 nm-thick coating of carbon. The microscope was run with an acceleration voltage of 15 kV and a probe current of 3 nA, a scan speed of 32 µs/pxl and under high vacuum in the analysis chamber. EDX maps covering large representative areas for each alteration zones of the two rocks were obtained, and the quantification of elemental chemistry was performed in various zones of these maps.

Three thin sections were analyzed using SEM-EDX: one for the ROR0311 sample and two for the Solund sample. Only one thin section was analyzed for ROR0311, as all the zones of interest were present in this section. For the Solund sample, two thin sections were needed to analyze all zones of interest: one thin section with the core and the alteration 1, and one thin section with the alteration 2.

Data were processed using the ESPRIT software. The SEM map has been divided into 349 squares of 1 mm². For each of these squares, an average EDX spectrum is calculated. For ROR0311, the chemistry has been estimated from the average of 4 squares for each zone of interest (core, alteration 1 and 2) (see Table 6 and Figure S22 in the supplementary material). For the Solund sample, only the two zones of the core and the alteration 2 were analyzed, using 3 squares for each of these two zones. The alteration 1 was not analyzed due to lack of data (see Table 6 and Figure S23 in the supplementary material). After adjusting the baseline, elements of interest were selected in this final spectrum and quantified based on the intensity of the relevant peaks in the analyzed zones. The absolute errors for the elements of interest are 0.46% (Si), 0.11% (Fe), 0.84% (Mg) and 0.002% (Ca).

The distribution of the different mineralogies using the SEM images is determined in the same way as with the micro-Raman images. The only difference is that for the SEM, the average of 3 images was processed (instead of one for the micro-Raman), representing an area of 3 mm<sup>2</sup>. However, this has been possible only for the ROR0311 sample. The Solund sample had too many different phases present in these SEM analyses, which made our methodology not applicable in this sample.

# 4. Results

For each sample, we present the advanced characterization using conventional laboratory techniques, SEM and micro-Raman, to provide specific characterization of our samples for comparison with the literature. Then, we present the data obtained with the SuperCam-like techniques: remote TR Raman, VISIR and LIBS.

# 4.1. ROR0311

# 4.1.1. Micro-Raman analyses

# Core of the peridotite

Fig. 2 presents two maps of the same region of the core of the peridotite, as well as representative spectra for each of the minerals observed in the map. For the maps, the spectra allow us to identify olivine with the peak doublet at  $820-860~\rm cm^{-1}$ . This doublet is characteristic of olivine and is due to coupled symmetric  $(v_1)$  and asymmetric  $(v_3)$  stretching modes in the  $SiO_4$  tetrahedron. Serpentine is also detected

Table 2
Main minerals detected with micro-Raman and SEM techniques.

Sample ROR0311				
Zones	Refs. [42]	Micro-Raman	SEM	
Core	41% serpentine 51% olivine 8% brucite	30% serpentine 61% olivine 8% brucite 1% iron oxide	45% serpentine 53% olivine 2% iron oxide	
Alteration 2	10% porosity	50% serpentine 35% olivine 15% porosity	51% serpentine 46% olivine 3% iron oxide	

by peaks at 230 and 384 cm<sup>-1</sup> as well as 688 cm<sup>-1</sup> corresponding to the vibration of Si-O-Si. Hydration is detected by a doublet peak at 3680–3700 cm<sup>-1</sup> due to the stretching vibration of OH bonds. Locally, some brucite is observed based on its hydration signature consisting of a doublet of peaks in the hydration region at lower wavenumber compared to serpentine, around 3640–3650 cm<sup>-1</sup>. Finally the iron oxides are detected with the large peak between 600 and 800 cm<sup>-1</sup>.

The map Fig. 2A/ depicts the mineralogy from the analysis of the  $100{\text -}1400~\text{cm}^{-1}$  spectral range while the map Fig. 2B/ depicts the hydration for the same area based on the analysis of the  $3200{\text -}3600~\text{cm}^{-1}$  spectral range. This zone exhibits large fractured olivine crystals (red) filled with serpentine (green). Additionally, brucite (blue) is detected inside some veins of serpentine, and a small amount of iron oxide (cyan) is also present. The second map, showing the  $OH - H_2O$  spectral range, enables us to distinguish brucite and serpentine by considering the relative intensity of the peaks at 3640 and 3650 cm $^{-1}$ , which is stronger for brucite.

## Alteration 2

The most altered section of the rock (alteration 2) has also been analyzed by Raman and is processed the same way as the core. Only the spectral range from 100 to  $1400~\rm cm^{-1}$  is presented here (Fig. 3).

Two mineral phases are detected in this map: olivine crystals and serpentine surrounding them, as well as a third feature located in the central of the serpentine veins (black). The olivine crystals are generally more fractured and smaller compared to those in the core of the rock. The spectrum associated with the third feature is represented in black in the lower figure and appears flat with no peak detected, indicating the absence of mineral phases. [42] discovered that in the altered part of ROR0311, brucite, which was detected in the core, is dissolved and replaced by porosity due to weathering. Therefore, the flat spectra in the black zones of the map correspond to void in the local porosity.

The mineral phase distribution throughout the rock has been analyzed using the micro-Raman and SEM maps. The results obtained are shown in Table 2. The SEM results are not as precise as the micro-Raman ones, because neither brucite nor porosity are detected. The results of the semi-quantification with the micro-Raman maps on the core of ROR0311 gives 30% serpentine, 61% olivine, 8% brucite and 1% iron oxide. For the alteration 2, we obtain 50% serpentine, 35% olivine and 15% porosity.

Moreover, the average Fo# of the olivines, calculated using the micro-Raman spectra, is Fo# =  $92 \pm 3$ . This value was obtained by analyzing eight spectra. This Fo# is consistent with the results of [41], which also report an Fo# of 92 based on electron microprobe analysis.

# 4.1.2. SEM-EDX analyses

The compositions obtained from the SEM-EDX analyses for each alteration phase of ROR0311 are presented in Fig. 4. From the core (almost unaltered) to the alteration 2, a decreasing trend for MgO and an increasing trend for  $\mathrm{SiO}_2$  are observed while the concentration of FeO remains stable across these zones.

The trend of molar (Fe+Mg)/Si is convenient and used on Mars to explore mafic minerals and some silicate alteration phases [20].

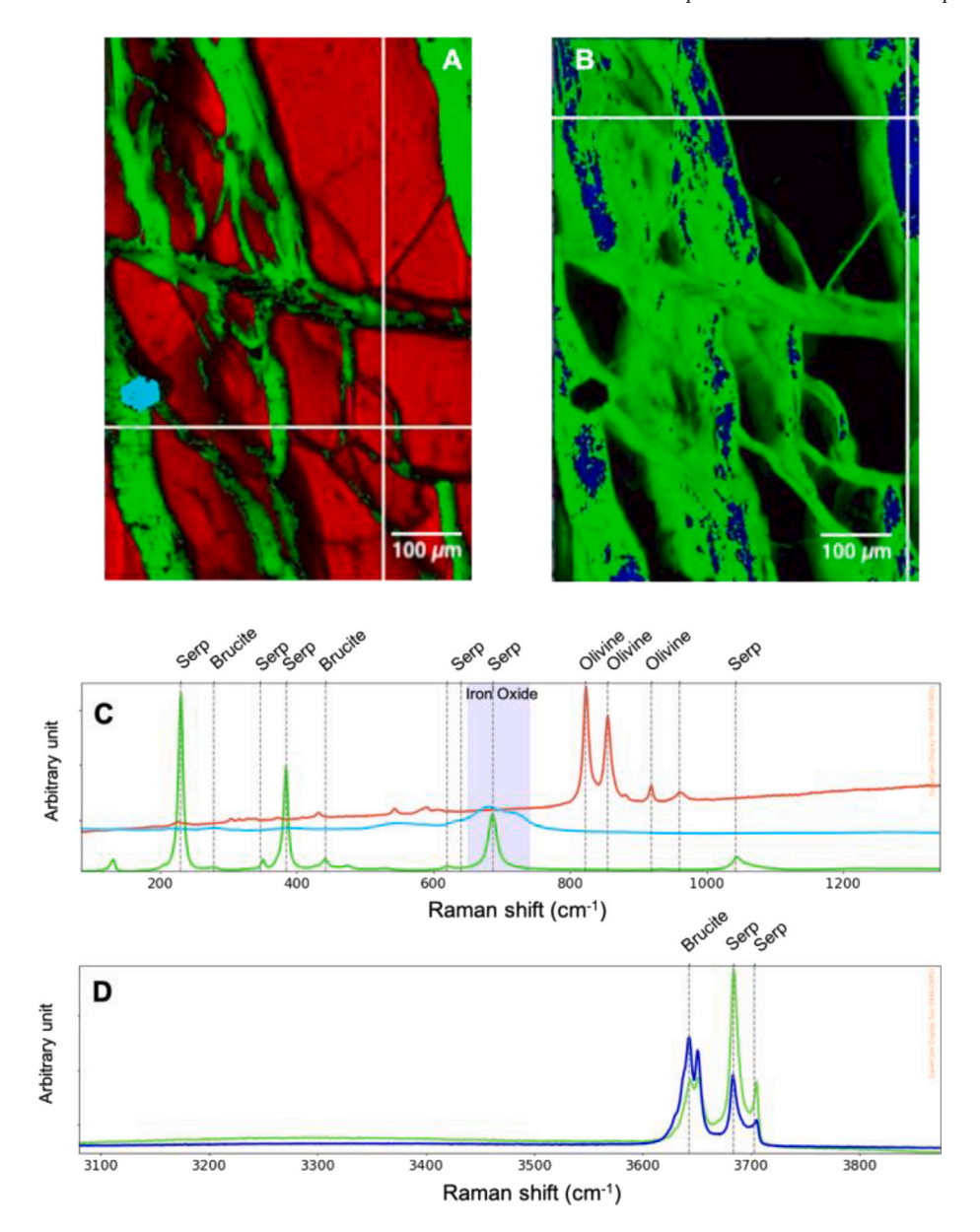


Fig. 2. Raman map and associated spectra of the core of sample ROR0311. Color code: red/black = olivine, green = serpentine, cyan = iron oxide, blue = brucite. A/ Map in the range 100 to 1300 cm<sup>-1</sup>; 484.9 × 720.2  $\mu$ m, 206 642 spectra, 1.3  $\mu$ m × 1.3  $\mu$ m sampling step. Note the mesh texture of olivine and serpentine assemblage. Olivine is present as large crystals with size ranging from submicrometric to about 500  $\mu$ m. B/ Map in the OH – H<sub>2</sub>O range 484.9 × 720.2  $\mu$ m, 206 642 spectra, 1.3 × 1.3 sampling step. Brucite is observed in the central parts of the serpentine veins. C/ Spectra in the range 100 to 1300 cm<sup>-1</sup> (no normalization, no offset) of the minerals highlighted in the map (B). D/ Spectra in the range OH – H<sub>2</sub>O (no normalization, no offset) of the minerals highlighted in the map (B).

Stoichiometrically, this ratio is 2 for a perfect olivine while it should be ideally 1.5 for serpentine.

As shown in Fig. 4, the core of the peridotite has an (Fe+Mg)/Si ratio close to 2, suggesting that olivine is the main mineralogical phase. The (Fe+Mg)/Si ratio is then lower in the alteration 2, suggesting a decrease in the amount of olivine and an increase in the amount of serpentine or other phases.

# 4.1.3. SuperCam-like Raman

Nine spots were analyzed on ROR0311 using the remote TR Raman, with three in each of the alteration zones (Figure S24 in supplementary material). The averaged spectrum for each zone is shown in Fig. 5. Olivine and serpentine are observed throughout the rock (with the spectral signature identified in the table S5 in the supplementary material). The serpentine signal, mostly in the hydration region, increases in the alteration zones whereas the olivine signal decreases. Brucite is

detected in the core, where a large peak at 3647 cm<sup>-1</sup> is more intense compared to the spectra in the altered zones where brucite has been dissolved. This broad peak corresponds to the doublet identified in micro-Raman but the two peaks are not completely resolved here because of the low spectral resolution. Overall, the spectra are relatively noisy, and the continuum is stronger, compared to the data obtained using the micro-Raman. This is expected since possible grain size effects and/or external light may affect the analysis in the remote TR Raman mode [43].

The average Fo# of the olivines calculated using the SuperCam-like Raman spectra is Fo = 92  $\pm 10$  by using 8 spectra covering the various zones. This is in agreement with the value obtained by micro-Raman and with literature data [41].

# 4.1.4. VISIR

Nine areas were analyzed on the sample (Figure S24 in supplementary material); their corresponding spectra are shown in Fig. 6-A. The

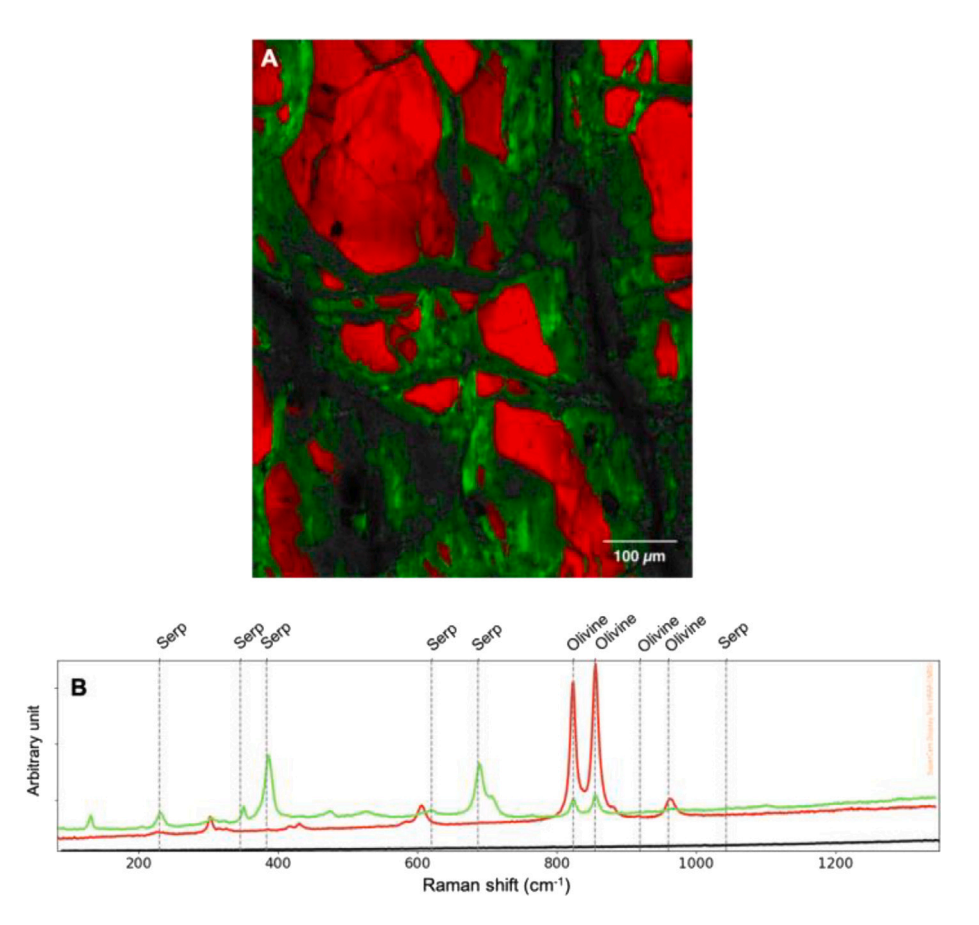


Fig. 3. Raman map and associated spectra of the alteration 2 of sample ROR0311. Color code : red = olivine, green = serpentine, black = porosity. A/ Map in the range 100 to 1300 cm $^{-1}$ ; 575.9 × 764.4  $\mu$ m, 260 484 spectra, 1.3  $\mu$ m × 1.3  $\mu$ m sampling step. Note the mesh texture of olivine and serpentine assemblage. Olivine is present in grain sizes from submicrometric to about 500  $\mu$ m. Porosity is observed in the central parts of the serpentine veins, reflecting the dissolution of brucite. B/ Spectra in the range 100 to 1300 cm $^{-1}$  (no normalization, no offset) of the minerals highlighted in the map (A).

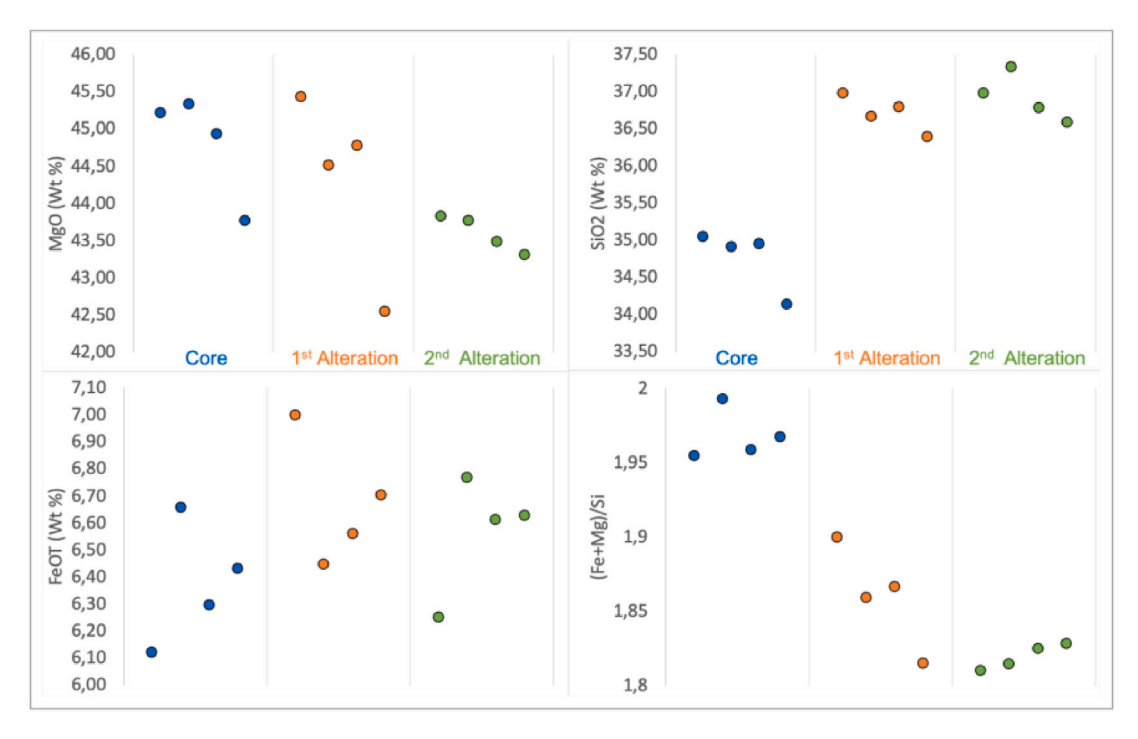


Fig. 4. SEM-EDX results obtained from the different regions of interest for ROR0311 sample. Each point corresponds to a 1 mm<sup>2</sup> square analysis (see Section 3.4).

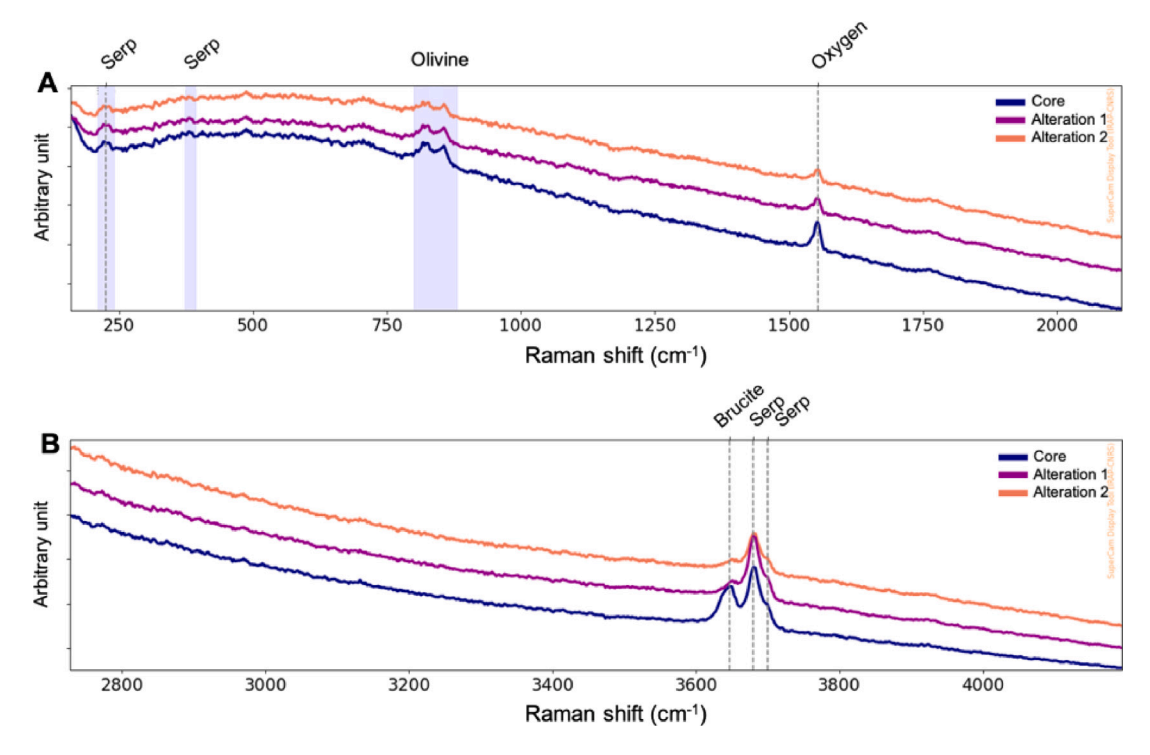


Fig. 5. Raman spectra of the three zones of ROR0311 conducted with the SuperCam-like Raman. The spectra corresponds to an average for each of the three zones: Core, Alteration 1 and Alteration 2. A total normalization and an offset were applied. The oxygen peak corresponds to the contribution of oxygen in the room.

spectra show an increase of reflectance with alteration. The serpentine signature absorption bands located at 1.39  $\mu m$ , 2.33  $\mu m$  and 2.5  $\mu m$  can be observed in most spectra. These bands correspond to the O-H groups bonded to magnesium cations. The depth of these bands increases with the alteration, which corresponds to the increase of proportion of serpentine from the core to the altered parts. The characteristic signature of olivine (large absorption band between 0.75  $\mu m$  and 1.5  $\mu m$ ) is absent from all spectra. For references, the typical spectra of the three main minerals in this sample are plotted in Fig. 6-B. The serpentine reference spectrum displays also a smaller band at 2.1  $\mu m$  that is unique to serpentine, but it is much more difficult to observe in mixtures.

# 4.1.5. LIBS

A total of twenty-three points were acquired on the ROR0311 sample in both the IRAP and LANL facilities: eleven in the core (unweathered part), and six in each of the two altered zones (Figure S24 in supplementary material). The average spectrum obtained for each part of the ROR0311 sample (core, alteration 1 and 2) with the instrument at IRAP is shown in Fig. 7. It can be observed that they are very similar to each other. The small variations between the different parts of the rock can be assessed by comparing the peak areas of the elements of interest, even though the relation between the LIBS signal and the elemental content is not necessarily linear as explained in Section 3.2.

The peak areas retrieved for each element of interest (Si, Mg, Fe, H) and for each setup are shown in Fig. 8 in gray. Signals obtained from both setups are very similar (only the absolute intensity differs, as explained in Section 3.2) and therefore a moving average is shown to highlight the possible trends and reduce the outliers. The Mg signal decreases slightly from the core to the second alteration, while the Fe and Si signals slightly increase, even though a lot of dispersion is observed. The H signal remains overall stable, with much more dispersion at IRAP (Fig. 8).

The quantitative results retrieved from the LANL dataset are shown in Fig. 9, for the same elements of interest. The concentration of MgO decreases and that of FeO is variable but overall constant from the core to the alteration 2. The  $SiO_2$  content is slightly higher in the alteration

2 only. These trends are overall consistent with the SEM-EDX results, as well as with the LIBS qualitative analysis. The main difference is about the Fe signal that seemed to increase from the core to the alteration 2 via the LIBS qualitative assessment, whereas it is stable from the SEM-EDX and quantitative LIBS results. These slight differences are discussed in Section 5.3.

ROR0311, as seen on the micro-Raman maps, exhibits large enough grains of olivine to conduct some stoichiometric ratios, assuming the LIBS laser sampled a single grain of olivine. Looking at the (Fe+Mg)/Si ratio 9, data are sparse for the core and the alteration 1, ranging from 1.45 to 1.93. This suggests that these zones actually include olivine and other phases and that they are heterogeneous with several phases being sampled. The alteration 2, on the other hand, shows a constant ratio at 1.5. The dispersion seems smaller compared to the core part reflecting less heterogeneity, which could confirm the presence of more serpentine in this part. The comparison with the SEM-EDX results is discussed in Section 5.3.

# 4.2. Solund

# 4.2.1. Micro-Raman analyses

# Core of the peridotite

Fig. 10 displays a map of the core of Solund and its associated spectra, where calcite and serpentine are detected, using the spectral range between 100 and  $1400~\rm cm^{-1}$ . Calcite is identified with the peaks at 1088, 154 and 281 cm<sup>-1</sup>. Micro-Raman analysis of the core of Solund revealed no evidence of olivine, but only serpentine, calcite and quartz. The absence of olivine may be due to the advanced stage of serpentinization in the sample studied.

# Alteration 2

The map and associated spectra from the most altered section of the Solund sample are presented in Fig. 11. The map displays three main phases: hematite in gray, talc in purple and calcite in yellow. Hematite is detected with its broad band at  $1317~\rm cm^{-1}$  and talc with its peaks at  $195~\rm cm^{-1}$  and at  $677~\rm cm^{-1}$ .

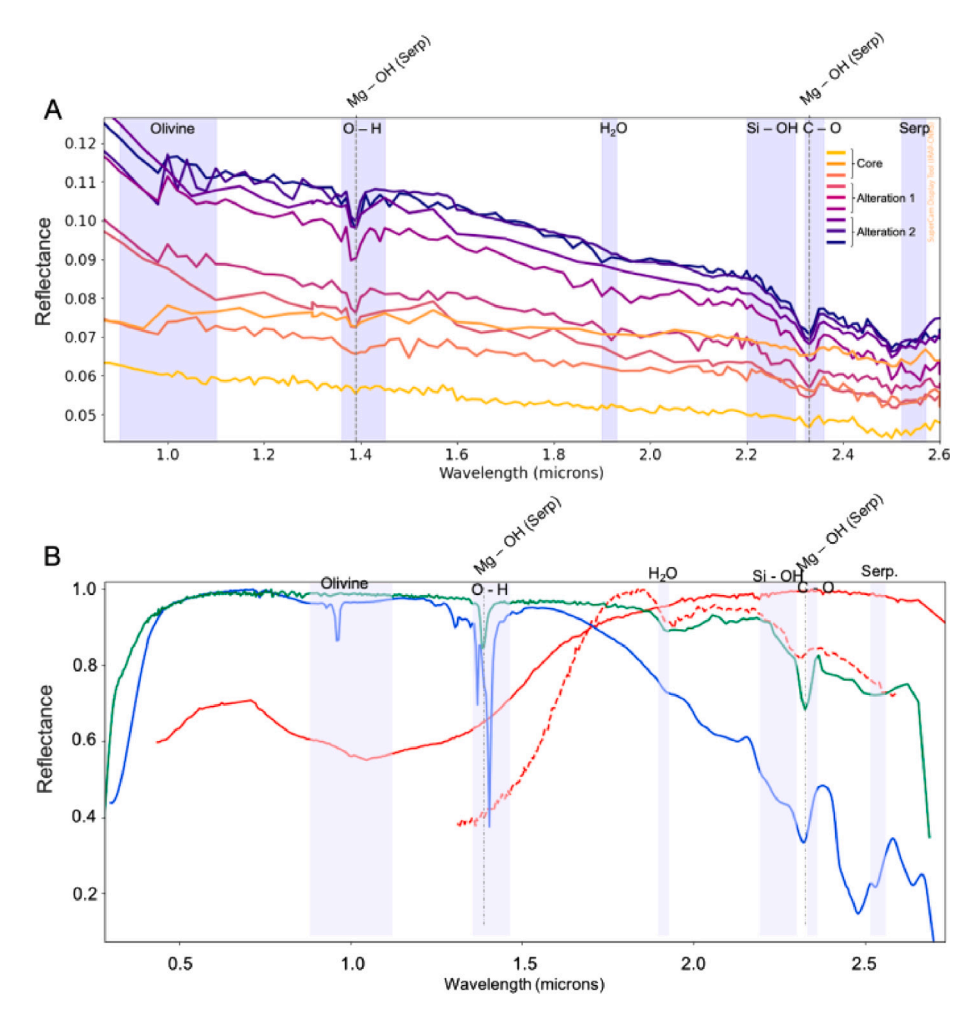


Fig. 6. (A) VISIR spectra from the core of ROR0311 (yellow) to the alteration 2 (purple). (B) Reference VISIR spectra from the CRISM spectra library [59,60], and an example of an olivine spectrum from Mars (target Cine, point 5) in dashed line. Color code: red = olivine, green = serpentine, blue = brucite. Spectra have been normalized to the maximum intensity. No offset has been applied.

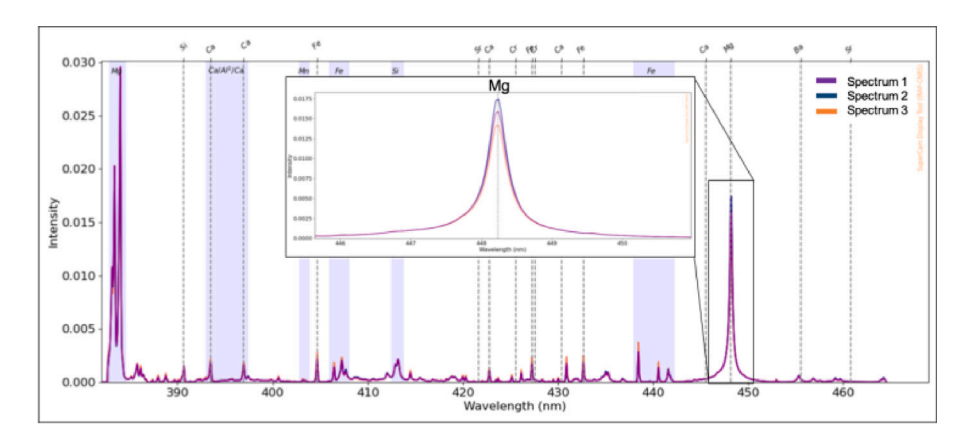


Fig. 7. LIBS spectra of the three areas of ROR0311 - taken in the VIO range - focus on the magnesium peak at 448 nm. Signals have been normalized by their total intensity of each associated range.

Serpentine is also present in the outer rim, but not in the specific zone shown on the map.

The results of the semi-quantification with the micro-Raman maps on the core of Solund gives: 65% of serpentine and 31% of calcite. For the alteration 2, we obtain 54% of hematite, 42% of talc and 4% of calcite.

# 4.2.2. SEM-EDX analyses

For the Solund sample (Fig. 12) the SEM-EDX data obtained from the core to the altered part show a slight decreasing trend for MgO. The  $\mathrm{SiO}_2$  content remains stable. Concerning CaO and FeO, there is a lot of dispersion in the alteration 2 part of the sample, with one point (over 3) being higher. Nevertheless, the CaO content seems to drop in

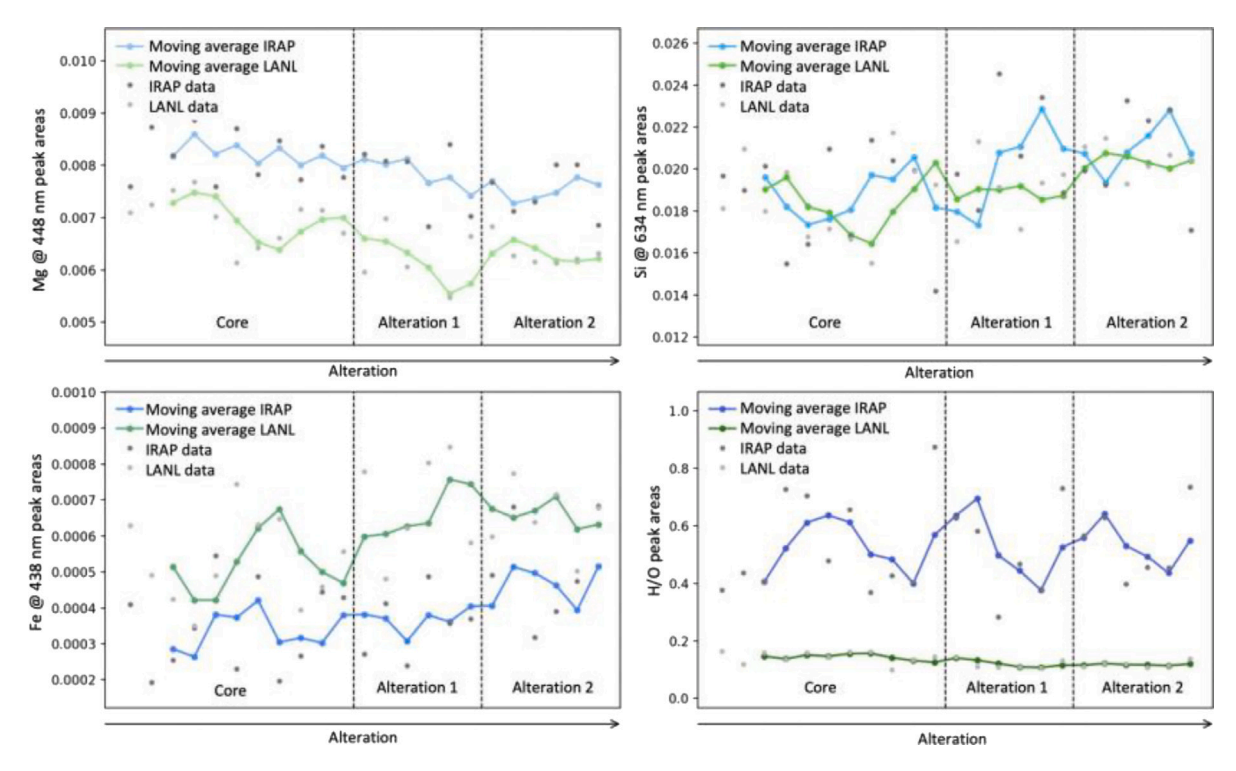


Fig. 8. Evolution of peak areas for Mg, Si, Fe and H/O in ROR0311. IRAP and LANL data are presented with their associated moving average. Signals have been normalized by their total intensity of each associated range.

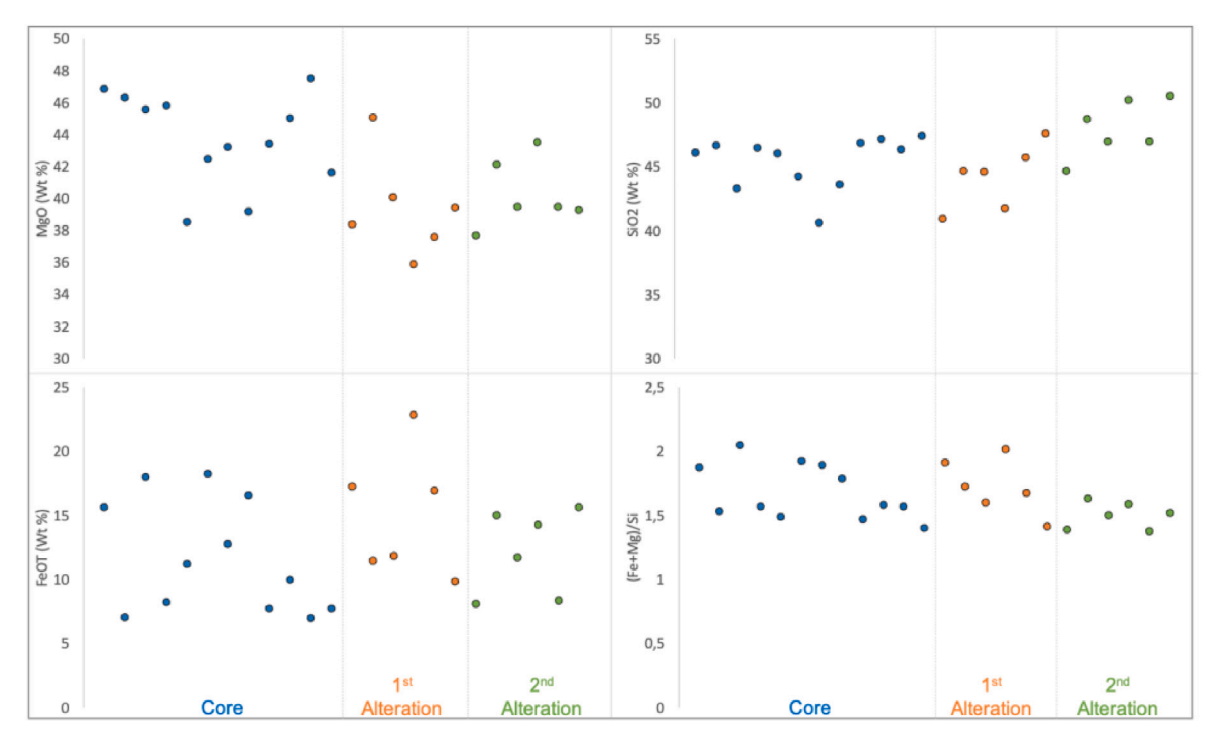


Fig. 9. Evolution of MgO, SiO<sub>2</sub>, FeO and (Fe+Mg)/Si in ROR0311 in the three phases of alteration obtained from the LIBS quantification. Each point corresponds to one point analysis (see Section 3.2).

the alteration 2. Overall, there is more dispersion for all the analyzed elements in the alteration 2, indicating a heterogeneous mineralogy in this part of the sample. The stoichiometric ratio of (Fe+Mg)/Si shows a relatively constant value between both areas that is in the range 1–1.6,

consistent with the absence of olivine and the presence of serpentine. Again, more dispersion is observed in the alteration 2, likely due to the small grain size and local strong heterogeneity. However, in terms of stoichiometry, it is not relevant to perform (Fe+Mg)/Si on this sample

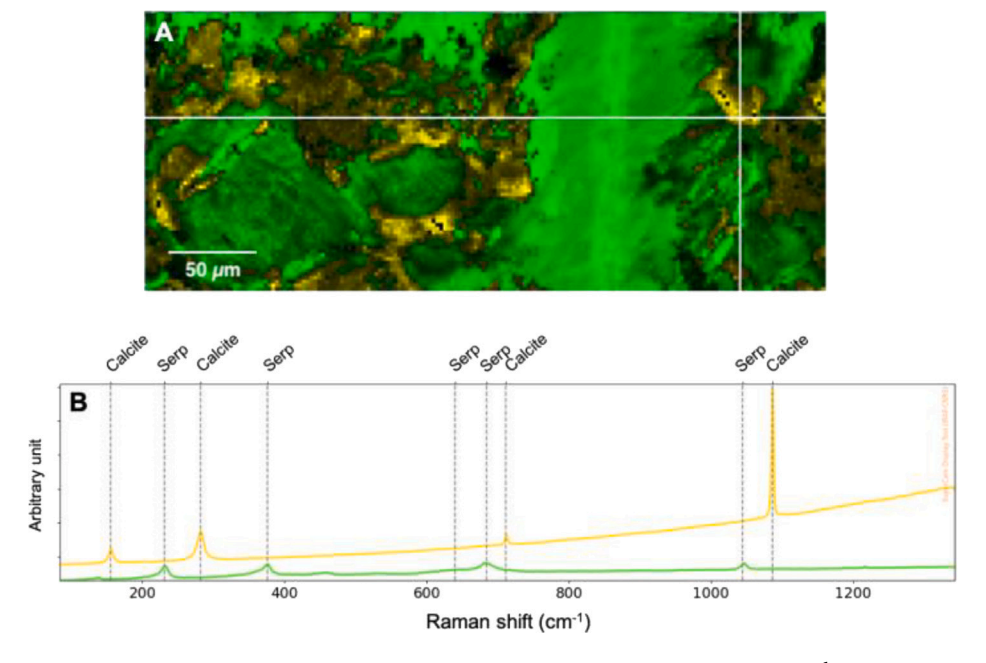


Fig. 10. Raman map and associated spectra of the core of sample Solund in the spectral range from 100 to 1400 cm $^{-1}$ . Color code: green = serpentine, yellow = calcite. A/ Map in the range 100 to 1400 cm $^{-1}$ ; 356 × 146  $\mu$ m, 12 994 spectra, 2  $\mu$ m × 2  $\mu$ m sampling step. Note the altered texture of the rock composed mostly by serpentine and calcite. B/ Spectra in the range 100 to 1400 cm $^{-1}$  (no normalization, an offset has been applied) of the minerals highlighted in the map (A).

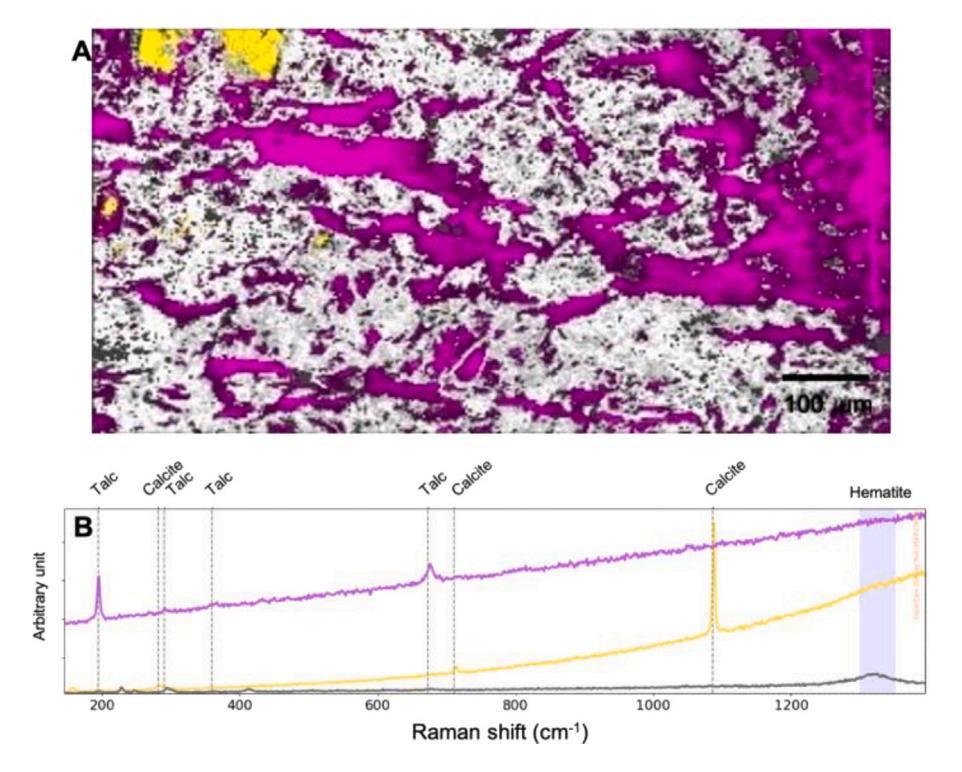


Fig. 11. Raman map and associated spectra of the alteration 2 of sample Solund. Spectral range analyzed : 100 to 1400 cm<sup>-1</sup>. Color code : yellow = calcite, purple = talc, gray = hematite. A/ Map in the range 100 to 1400 cm<sup>-1</sup>;  $1060.8 \times 538.2 \ \mu m$ , 84 456 spectra,  $2.6 \ \mu m \times 2.6 \ \mu m$  sampling step. B/ Spectra in the range 100 to 1400 cm<sup>-1</sup> (no normalization, no offset) of the minerals highlighted in the map (A).

because the size of the mineralogical phases are too small, and, thus, when looking at a  $1~\rm mm^2$  portion of the thin section, several phases are encountered (Figure S21 in supplementary material).

# 4.2.3. Remote TR Raman

Thirteen points were analyzed on Solund, two in the less altered core, three in the alteration 1 zone and eight in the alteration 2

zone (Figure S25 in supplementary material). Overall, the spectra are relatively noisy. Spectral data are presented in Fig. 13. Data from the core show evidence of serpentine and calcite despite the low signal-to-noise ratio of the spectra. In the alteration 1, talc, calcite and serpentine are detected. For the alteration 2, we have acquired data in two different areas - some in the bulk grey area, and others were obtained specifically in the hematite-rich red area (see Figure S21 in

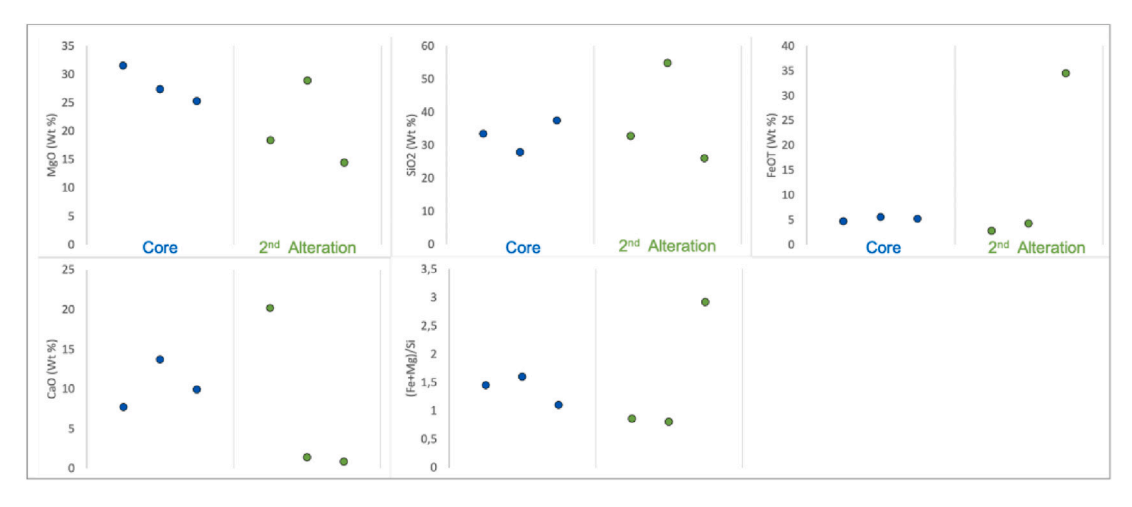


Fig. 12. SEM-EDX results obtained from the different regions of interest for Solund sample. Each point corresponds to a 1 mm<sup>2</sup> square analysis (see Section 3.4).

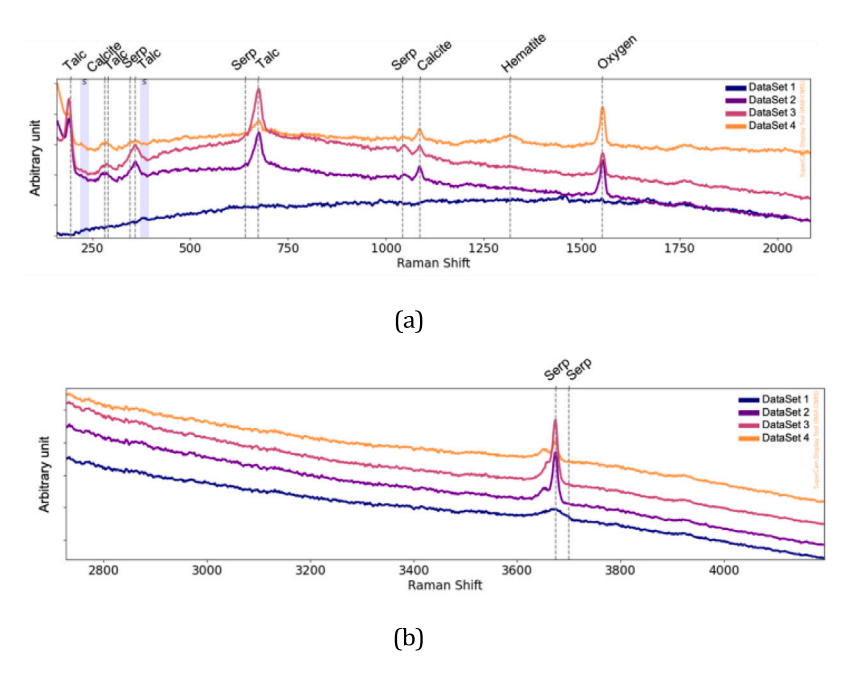


Fig. 13. Raman spectra of the four zones of Solund conducted with the SuperCam-like Raman. Each spectrum corresponds to an average of several spectra in each zones. Spectra are normalized and offset for clarity.

the supplementary material). In the grey area of the alteration 2, talc, calcite and serpentine are observed. In the red-part of alteration 2, the same minerals are detected, with an additional peak at  $1317~\rm cm^{-1}$  indicating hematite.

# 4.2.4. VISIR

As for ROR0311, nine regions in the sample were analyzed (Figure S25 in supplementary material) and their spectra are plotted in Fig. 14. Spectra acquired on Solund have a low reflectance (< 0.1) and present no obvious absorption bands (Fig. 14/a). Only the spectrum from the hematite-rich area of the sample has a higher reflectance and clear absorption bands, around 0.9  $\mu m$  that can be attributed to hematite, and sharp bands around 1.4 and 2.3  $\mu m$  that are consistent with talc (Fig. 14/b). For reference, the typical spectra of the three main minerals in this sample are plotted in Fig. 14/c. The absorption bands of calcite may overlap with those of serpentine, particularly the one at 2.34  $\mu m$ . Nevertheless, serpentine can still be distinguished, as its spectrum exhibits three characteristic absorption bands at 1.39  $\mu m$ , 2.33  $\mu m$ , and 2.50  $\mu m$ . In contrast, calcite shows a stronger absorption feature at 2.55  $\mu m$  than at 2.34  $\mu m$ . By analyzing the position and intensity ratio of

the 2.34  $\mu m$  and 2.55  $\mu m$  bands, along with the presence or absence of the 1.39  $\mu m$  band, it is possible to differentiate serpentine from calcite.

# 4.2.5. LIBS

Twenty-one LIBS points were observed on Solund at both the IRAP and LANL facilities. Eight are located in the core, five in the alteration 1 and eight in the alteration 2 (Figure S25 in supplementary material). The spectra are shown in Fig. 15, with a close-up on the Mg peak in the VIO range, where an increase in its intensity with increasing alteration is observed.

Fig. 16 shows the peak areas of the elements of interest as a function of the alteration of the rock. In this sample, the Mg and Si LIBS intensities increase with the alteration. Fe LIBS signal remains overall stable, even though large variations are observed in the alteration 2 part. H/O results tend to decrease from the core to the alteration 2, with both setups, even though the absolute signal for H/O cannot be compared between the setups, as explained in Section 3.2.

With the LIBS techniques, carbonates are often investigated using their C/O signal, as described in [55] and applied in [21]. Fig. 17 shows the values of C/O using the peak areas from both setups. This ratio is

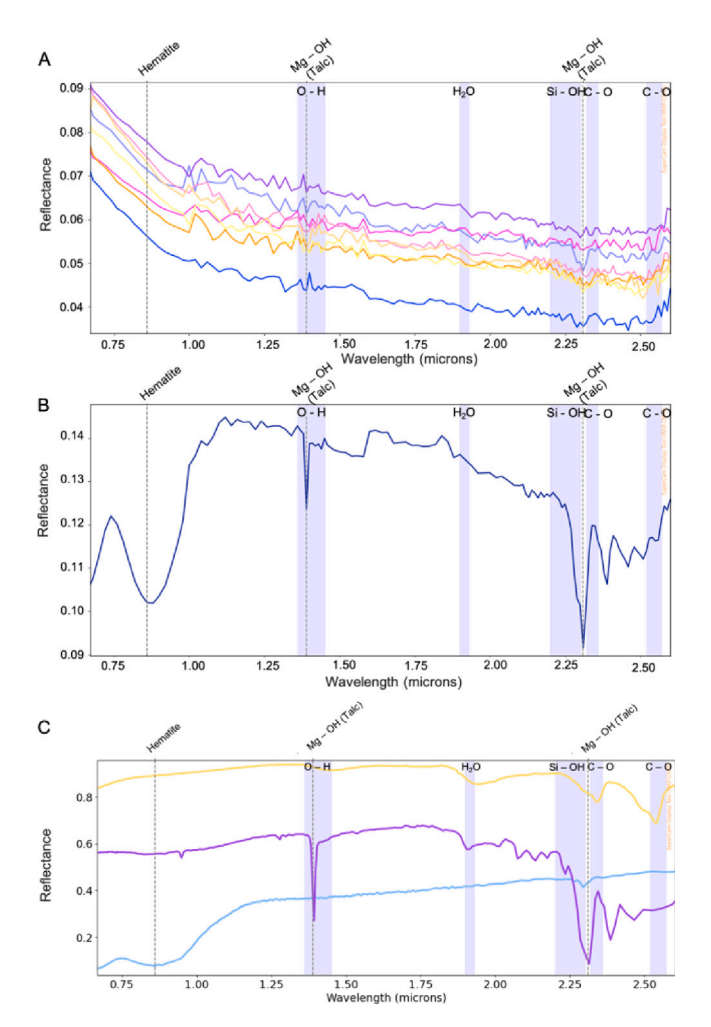


**Fig. 14.** (a) VISIR spectra from the core of Solund (yellow colors) to the alteration 2 (purple/blue colors). (b) VISIR spectra from the hematite area of Solund. (c) Reference VISIR spectra from the CRISM spectra library [59,60]. Color code: calcite = orange, talc = purple, hematite = dark blue. Spectra have been normalized to the maximum intensity. No offset has been applied.

overall constant between the core and alteration 1. However, there is a decrease in alteration 2 that is well observed in the IRAP setup, but less pronounced in the data from LANL. As with the H/O ratio, only the trends can be compared for the C/O, as explained in Section 3.2.

Fig. 18 shows the evolution of the averaged concentration retrieved from the LIBS data of MgO,  $\mathrm{SiO}_2$ , FeO and CaO between the three areas of the rock. The concentration of SiO2 increases considerably from the core to the alteration 2 while the one of FeO is the lowest in alteration 2. The evolution of MgO is complex, with a decrease from the core to the alteration 1, but a content slightly higher in alteration 2 compared to the core. CaO has a particular behavior, as its content drops nearly to zero in alteration 2. This could be explained by the fact that in the core and alteration 1, some calcite was observed from the Raman observations (and as reported in [40-42]). These observations, combined with that of the evolution of C/O, suggest a decreasing amount of carbonate in the last weathered phase. Besides the Si trend, these LIBS quantitative results do not necessarily match the observations from the qualitative analysis. Indeed, the trend observed in Mg content is less pronounced than the one from the Mg peak areas (as seen in Fig. 16). The biggest difference is observed for the Fe signal. From the qualitative observation (Fig. 16), the Fe peak area is overall stable from the core to alteration 1, with much more dispersion in alteration 2 and a few points clearly lower than any other. This heterogeneity in alteration 2 was

Table 3

Summary table obtained with the three SuperCam techniques on ROR0311 samples. For LIBS results, a combination of quantitative data and peak areas are presented. The literature section is a summary of the results presented in [40–42]. "+" means the presence of the element/mineral. "-" means the presence of the element/mineral, but to a lesser extent. "N/D" means that the mineral has not been detected.

	Sa	ample ROR03	311	
	Mineral	Core	Alteration 1	Alteration 2
	olivine	+	+	+
	serpentine	+	+	+
Literature	chromite	-	-	-
	brucite	+	N/D	N/D
	porosity	N/D	N/D	+
TRR	olivine	++	+	_
	serpentine	+	+	+
	brucite	+	N/D	N/D
VISIR	serpentine	-	+	++
LIBS	Mg	++	+	-
	Fe	_	+	+
	Si	_	-	+
	(Fe+Mg)/Si	+	+	-

also noticed from the SEM-EDX analyses. However, the predicted LIBS content for FeO drops for most of the points in alteration 2 compared to the core and alteration 1, which is different from what is observed from the peak areas. As explained in Section 3.2, here we are looking at only one Fe peak, whereas the quantitative model uses all the Fe lines from the entire spectral range. This sample also presents some abrupt variations in mineralogical assemblages, with a clear drop in calcite content in alteration 2 (as seen in Section 4.2.1). This drop in calcite content could bias our Fe peak areas (and probably the Mg peak selected as well), due to the way we normalize the spectra. Indeed, the lower total intensity due to less Ca lines could then enhance the signal of the remaining elements (such as Fe and Mg), compared to their signal in the core or alteration 1, where the calcite content was at a higher level. This should not affect the Si qualitative assessment, as its elemental line selected is from another spectral range, where much fewer Ca emission peaks are present, affecting much less the normalization. Nevertheless, besides the trends, the quantitative values are not entirely consistent with those from the SEM-EDX data and this is discussed in Section 5.3.

Solund exhibits mineral phases that are overall smaller than the LIBS spot size, with a fine-grained mesh texture (Figs. 10, 11). Therefore, stoichiometric analyses cannot be performed directly, as the LIBS point will sample a mixture of phases (see part 4.2.2). In that case, as shown with the SEM results in part 4.2.2, the (Fe+Mg)/Si ratio should be used with caution. Indeed, this ratio is lower in the alteration 2, not because of the higher presence of serpentine, but because the Si content in that area is much higher compared to that of the core and alteration 1, due to its enrichment in talc.

# 5. Discussion

Each technique (LIBS, VISIR, Raman, SEM-EDX and micro-raman) used in this study has its own specificity (footprint size, sensitivity, etc.) that needs to be discussed, in order to better compare and interpret the results. In particular, the combination of LIBS and Raman for planetary exploration has long been investigated as these two techniques have the same instrumental architecture and are complementary in terms of scientific input [61,62]. Results obtained with the SuperCam techniques are compared to the litterature for discussion, for both samples (see Tables 3 and 4)

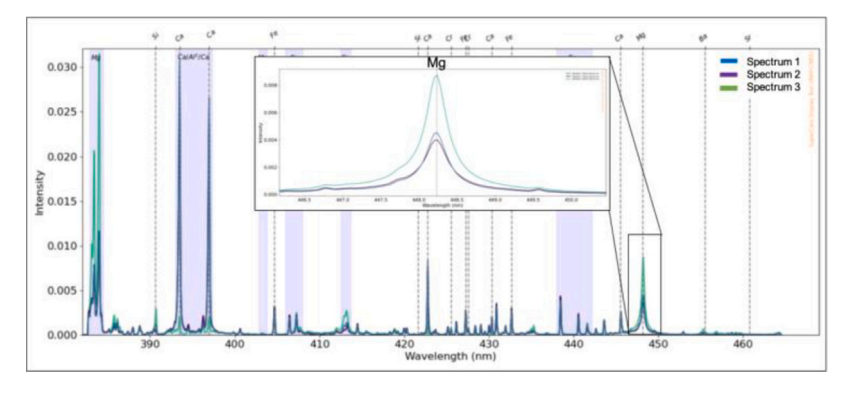


Fig. 15. LIBS spectra of the three areas of Solund. The VIO spectral range is shown; the inset shows a close-up view of the magnesium peak at 448 nm. Signals have been normalized by their total intensity of each associated range.

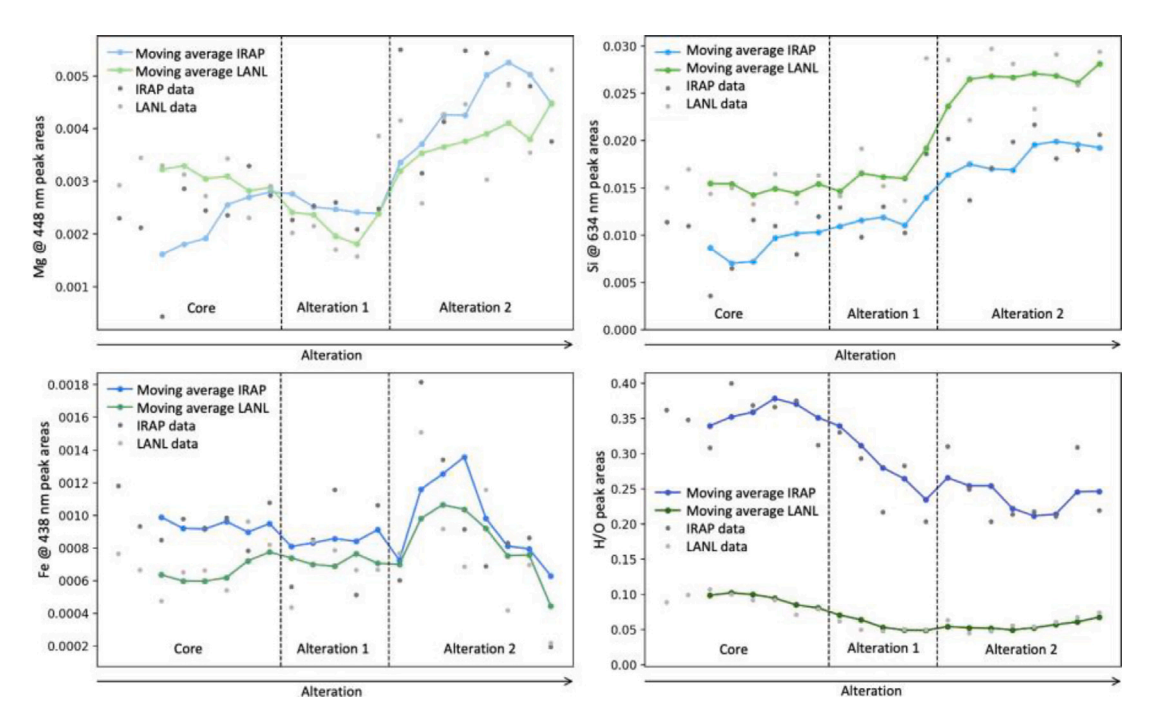


Fig. 16. Evolution of peak areas for Mg, Si, Fe and H/O in Solund. IRAP and LANL data are presented with their associated moving average. Signals have been normalized by their total intensity of each associated range.

# 5.1. Performance of Raman spectroscopy

It is important to stress that remote TR Raman is quite different compared to laboratory commercial microspectrometers like the Renishaw InVia system used in this study. First, SuperCam Raman performs remote analysis whereas commercial Raman systems mostly do micro-analysis, involving a difference in footprint between the two techniques (in the micron range for the commercial Raman systems versus 5 mm for the TR Raman in this study). Therefore, laboratory instruments generally probe a single mineral phase while SuperCam will likely probe a population of minerals depending on grain size. However, SuperCam can perform analyses from several meters away, which results in significant operational efficiencies for the rover.

A second major difference is that nearly all commercial instruments use continuous-wave laser excitation while SuperCam is a time-resolved instrument using a pulsed laser synchronized with a gated detector. The idea is that the Raman signal (lifetime  $\approx 10^{-14}$  s) will last only during the excitation pulse, while other signals like luminescence (lifetime  $> 10^{-9}$  s) will be excited by the pulse but will continue to decay after it. Using a short(-time) gate (100 ns for SuperCam) that is synchronized

with the laser pulse allows efficient rejection of parasitic signals like luminescence or daylight entering the telescope and maximization of the Raman signal. Compared to continuous-wave instruments, SuperCam Raman benefits from signal intensification and filtering in the time-domain but uses considerably less excitation, hence receives less signal because of the non continuous excitation.

In sample ROR0311, the SuperCam-like Raman detects all the expected mineral phases detected by the micro-Raman survey, as described by [42]. In particular, it detects brucite which is not observed by either LIBS or VISIR and this is a key detection to help interpreting the chemical data and their variation in SEM-EDX and LIBS data.

On Mars, up to the crater rim, SuperCam has detected olivine and carbonates in more than 20 rocks [20,21] via the Raman technique. In both cases, the signal was good enough to retrieve chemical information based on peak position [20,21,31]. However no serpentine or Mg-rich phyllosilicates has been directly identified from the Raman spectra. This is likely due to the scarcity of these phases in the Martian rocks analyzed so far as they were not detected by VISIR also, and/or to their small grain size that makes them challenging to detect with Raman. In addition, on Mars, the usual setting corresponds to 400 laser shots per point which is considerably lower than the 200 000 to 500

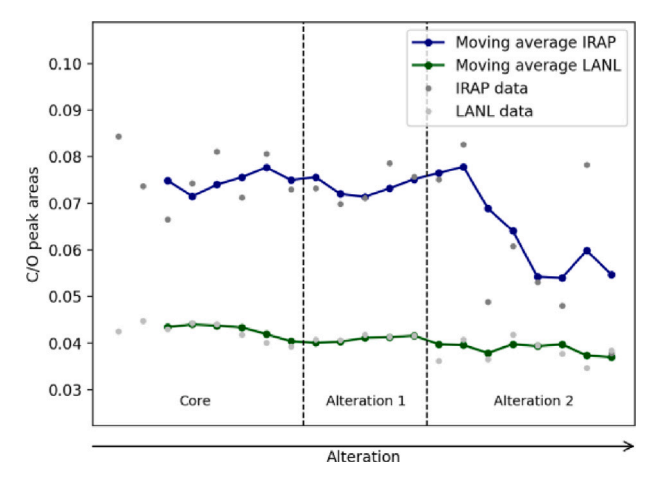


**Fig. 17.** Evolution of C/O peak areas in Solund. IRAP and LANL data are presented with their associated moving average. Signals have been normalized by their total intensity of each associated range.

# Table 4 Summary table obtained with the three SuperCam techniques on Solund samples. For LIBS results, a combination of quantitative data and peak areas are presented. The literature section is a summary of the results presented in [40–42]. "+" means the presence of the element/mineral. "-" means the presence of the element/mineral, but to a lesser extent. "N/D" means that the mineral has not been detected.

		Sample Solun	d	
	Mineral	Core	Alteration 1	Alteration 2
Literature	olivine	+	N/D	N/D
	serpentine	+	+	N/D
	chromite	+	N/D	N/D
	quartz	+	N/D	+
	dolomite	+	N/D	N/D
	magnesite	+	N/D	N/D
	magnetite	+	N/D	N/D
	calcite	N/D	+	+
	talc	N/D	+	+
	hematite	N/D	N/D	+
TRR	serpentine	+	++	++
	calcite	N/D	+	+
	talc	N/D	++	+++
	hematite	N/D	N/D	+
VISIR	serpentine	N/D	N/D	+
	hematite	N/D	N/D	++
	talc	N/D	N/D	++
LIBS	Mg	-	+	++
	Fe	+	+	-
	Si	-	+	++
	Ca	+	++	_
	(Fe+Mg)/Si	++	+	_

000 shots used for the SuperCam-like instrument in the laboratory. This significant difference in the number of shots can explain the easier and better detection of alteration phases like serpentines or phyllosilicates in the laboratory. Indeed, when using 400 shots in the laboratory on ROR0311, no olivine was detected while the rock is composed of 50 to 60% of this mineral, with a grain size of a few hundred microns. On the other hand, SuperCam Raman on Mars in the Séitah unit was able to detect olivine even with only 400 shots [20]. This is probably due to the cumulate texture of these rocks composed dominantly by millimetric grains of olivine, allowing the analytical footprint to observe only this single mineral phase.

Laboratory and SuperCam-like Raman data from ROR0311 yield a Fo# of about 92 for the two instruments. This value is in excellent agreement with the Fo# 91–92 obtained by [41] based on electron microprobe data. A same approach was applied to the Martian data

by [20] yielding Fo# in good agreement with LIBS chemical data. A similar approach was recently applied for the carbonates in the margin units and the Fe-Mg composition of carbonates estimated from the position of the nu1 peak is in agreement with the estimation based on LIBS data [31].

# 5.2. Performance of VISIR spectroscopy

VISIR spectra of ROR0311 do not exhibit the expected detections. Indeed, olivine, which comprises a significant fraction of the sample at approximately 60% in the core and 35%–40% in the alteration 2 zone, is not observed via the infrared instrument (Fig. 6). This is somewhat surprising since olivine is easily detected on Mars with the SuperCam infrared instrument either in bedrocks or in regolith [20,27]. The question raised is then, why is the primary and dominant mineralogical phase not observed with the VISIR in the laboratory?

The analyzed surfaces are saw cut, and the presence of coatings or rinds [63,64] can be excluded as a mechanism to explain the blue slope and lack of absorption band in the spectra of the rocks. The presence of a bluer slope for measurement obtained on rocks than that on powder has been observed in several studies [65–67], without a wellaccepted explanation at the moment. This increase in reflected light at lower wavelength should not be related to the refractive index, that is relatively constant for silicate in this spectral range. The increased reflectivity at lower wavelength could rather be due to the presence of wavelength scale roughness, leading to enhanced scattering of the lower wavelength. While [67] found that reflectance spectra of rocks have weaker absorption bands than related powders, they did not show such a disappearance of absorption bands. On the other hand, a similar behavior was observed by [65], in the case of rocks with reflectance < 0.1, as is the case of ROR0311. This effect was explained by a "weak surface scattering" regime, for which the reflected light is dominated by the first reflection on the slab surface (almost all photons that enter the rock are absorbed by opaques). Given the low reflectance measured, we propose that we are in a similar regime for ROR0311. Moreover, the olivine in this sample has a Fo# of 92, which means it is mostly Mg-rich and low in Fe content. As the slope between  $1.5-1.8 \mu m$  (used to detect olivine) is mostly related to Fe2+, this could explain why the olivine on the ROR0311 sample has not been detected with VISIR. Interestingly however, although olivine is not detected, the signatures of phyllosilicates are weak but visible (Fig. 6). Having accurate optical constant of serpentine may help understand if this is due to grain-size, intrinsic strength of the olivine and -OH bands, or a combination of the

# 5.3. Performance of LIBS

In contrast to Raman and VISIR spectroscopy, LIBS yields elemental rather than direct mineralogical information. As a result, mineralogical interpretation relies on indirect approaches such as stoichiometric calculation [19,20] or analysis of elemental correlations in sequential laser shots, as demonstrated in ChemCam studies on Mars (e.g., [68–70]). Distinguishing between different mineralogical phases is therefore facilitated if their compositions are really distinct, but is more challenging when the different phases are made of the same elements, as in the case with olivine and serpentine.

With its small analytical footprint compared to SuperCam Raman and VISIR, the LIBS technique can however detect small ( $<300~\mu m$ ) or minor phases. In this study, in the Solund sample, the change in calcite content was detected via the decrease in CaO content in alteration 2 compared to that of the core, both in LIBS and SEM-EDX data, even though a strong heterogeneity was observed. The C/O ratio of this target also showed a decreasing trend between the alteration 1 and 2. These two elements (Ca and C) are not part of the structural composition of olivine or serpentine and this observation is an important clue about the presence of calcite in the sample.

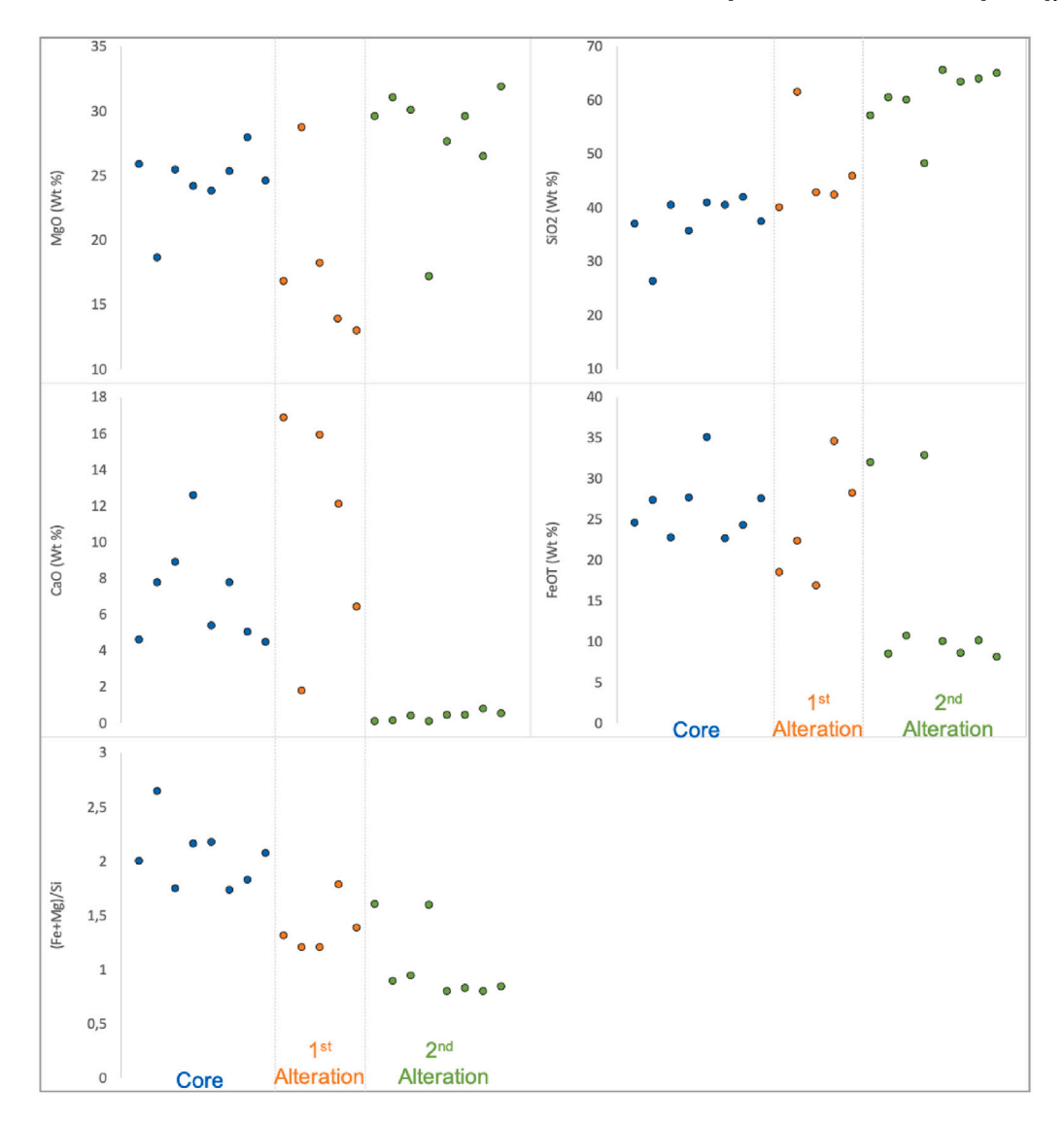


Fig. 18. Evolution of MgO, SiO<sub>2</sub>, FeO, CaO and Fe+Mg/Si in Solund in the three zones of alteration obtained from the LIBS quantification. Each point corresponds to one point analysis (see Section 3.2).

On the other hand, a stoichiometric approach can help deciphering between olivine and serpentine mineralogies by using the (Fe+Mg)/Si ratio, taking into account the different textures or grain sizes of the samples. Besides the stoichiometric approach, the H signal could be a good proxy to detect the presence (or variation in content) of secondary hydrated material. One could expect to see an increase of H from the less altered core to the most weathered alteration 2. However, in ROR0311, brucite is present in the core, and replaced by porosity in the alteration 2 zone, which may explain the nearly constant H signal along the transect (from core to alteration 2). Moreover, on natural samples, the H signal in LIBS spectra can be biased by a roughness effect, that tends to enhance the H peak intensity when the LIBS footprint falls into a groove or a small hole in the target [71]. This roughness effect is usually compensated when comparing similar rock types and textures to each other's, or also when using many data points to identify a main trend.

Some differences between the LIBS predictions and SEM-EDX results are observed (especially for the Solund sample), and can be explained by two considerations. First, the footprints considered for chemical quantification are different, much smaller for LIBS compared to that of the SEM-EDX (see Section 3.4 for details). Therefore, the SEM-EDX technique incorporates many more grains and therefore includes assemblages of several mineral phases in its analysis, whereas the LIBS

will tend to observe less mixture, and even probably sometimes will probe single grains of a given phase. Second, the sample itself was different for the LIBS and SEM-EDX analyses: rock sample for LIBS, and thin section for SEM. The thin sections are made from the counterpart of the sample, so should be relatively similar to it, but there is not a perfect match. However, the samples are somewhat heterogeneous with a spatial zonation-like structure of the alteration, especially the Solund sample (see Section 4.2.1).

Besides the differences related to the intrinsic heterogeneity of the samples, some differences are related to biases for each technique. This is probably the case for the  $\mathrm{SiO}_2$  content in ROR0311, that is higher from the LIBS quantification compared to that from the SEM in the core ( $\approx$  44 vs 35 wt%, resp.). This can be explained by the fact that the quantification from LIBS tends to overpredict the  $\mathrm{SiO}_2$  content in olivine-rich samples on Mars, as shown in [20,49]. The  $\mathrm{SiO}_2$  content is also higher from the LIBS data (compared to that of the SEM-EDX) in the alteration 2 of Solund ( $\approx$  60 vs 37 wt%, resp.). Nevertheless, we can also observe in Fig. 12 that in the alteration 2 of Solund,  $\mathrm{SiO}_2$  SEM-EDX data are much more variable (Fig. 18). There is no known bias for the  $\mathrm{SiO}_2$  predictions from LIBS on talc and serpentine. This high  $\mathrm{SiO}_2$  content from LIBS would suggest that the LIBS footprint mainly sampled some talc compared to the SEM-EDX. This hypothesis is supported by the micro-Raman map performed

on the thin section used for the SEM-EDX analyses (Fig. 11), where hematite is the dominant phase. Therefore, the SEM-EDX analyses might represent an area mainly composed of hematite (mixed with some talc). This would explain the higher dispersion observed for all the elements in alteration 2 of Solund, along with the differences between the SEM-EDX and LIBS data in this sample.

Whether using the LIBS quantification or the LIBS spectra, olivine and serpentine can hardly be distinguished as mentioned above. This is where the synergy between all the SuperCam techniques becomes essential.

# 5.4. Benefit of the synergy between the techniques

The three SuperCam techniques are not based on the same physical signal: while Raman and infrared spectroscopy are vibrational spectroscopy techniques, LIBS is an atomic emission spectroscopy. In this way, they complement each other and allow a variety of information to be compared in order to draw conclusions.

Comparing directly the results obtained with the three SuperCamlike techniques is challenging, first because their analytical footprints are different: 5 to 8 mm for VISIR, about 5 mm for Raman (in laboratory) and 0.45 mm for LIBS (for a target at equal distance of 7 m) [14]. Similar differences in the size of the analytical footprints are valid for SuperCam on Mars. The smaller LIBS footprint allows it to be less biased by mixtures, whereas the infrared and Raman techniques have more possibilities to analyze a combination of phases, making the interpretations highly dependent on the grain size of the analyzed target.

LIBS data help interpret the Raman data via the chemical quantification (it gives the information about which cation is present in the mineral structure [72]). However, the LIBS technique itself can hardly distinguish minerals with an overall similar elemental composition (olivine and serpentine for instance), as those are often mixed together at the micrometric scale.

VISIR observations, when combined with Raman analyses, confirm the presence of serpentine and its increasing abundance in the most altered part of the sample ROR0311. Nevertheless, VISIR data obtained for this specific study did not detect olivine (even though on Mars olivine is easily detected by this technique [17,20,27]). Without considering the Raman results, the detection of brucite becomes impossible, and thus the understanding of the LIBS quantification results is more difficult (in particular the H/O trend). The only indicator of brucite in the LIBS quantification was the decrease of magnesium between the core and the alteration 1, which could be explained by the dissolution of brucite and its replacement by porosity. On the other hand, Raman, unlike LIBS, cannot detect small changes in mineral quantification.

In the Solund sample, carbonates (calcite) were identified by Raman, and calcium was detected with LIBS. To understand the possible link between the observation of the two techniques, the LIBS C/O ratio was analyzed and gave the results shown in Fig. 17. The decreasing trend observed from the core to the alteration 2 could mean that the calcite content was decreasing.

The two analyzed samples, whilst they were altered through similar processes, show differences in terms of mineralogical assemblage. Taking into account the results for both samples, we observe that in one case olivine coexists with serpentine, whereas in the second case, only serpentine and other alteration phases are detected. The mineral phases, being dependent on the degree of alteration, can be very different from one protolith rock to another, even if these rocks are originally similar and have undergone the same types of alteration. Thus, differentiating olivine from alteration phases such as serpentine, brucite and calcite would be possible using Raman, with their distinct signature, whereas it would be much more challenging with only the LIBS technique to have one criteria that would work for all mafic rocks. On the other hand, thanks to the synergy between the different techniques of SuperCam, we have shown that it is possible to detect

and distinguish the different major and secondary phases of these two samples, and therefore highlight their differences in alteration stage.

A future work would be to investigate the use of data fusion between the LIBS, Raman and VISIR techniques for such kind of dataset. Indeed, several studies have already shown the advantages of such approach in planetary sciences (at least between the LIBS and Raman techniques), either at low-level (combination of spectra at the data level [73,74]) or by selecting specific variables per data type prior to concatenate the datasets [75]. However, these tests are usually performed using linear mixtures of specific compositions that are relatively easy to distinguish, and whereas it could be more difficult on these complex natural samples.

# 6. Perspectives

In the next decades, the planned landed missions to Mars already include Raman and Infrared with the ESA/ExoMars Rosalind Franklin rover. The Raman Laser Spectrometer (RLS - [76]) and MicrOmega IR imager [67,77] are accommodated inside the rover and will analyze powdered samples collected by the rover arm/drill. This mode of operation is different from SuperCam where VISIR and Raman are performed in remote sensing following a reconnaissance approach, with fields of view significantly larger than what will be achieved by ExoMars. The higher spatial resolution (about 20  $\mu m$  for MicrOmega and 50  $\mu m$ for RLS) should enable a better spatial unmixing of constituents, an improved understanding of vibrational signatures and a better control for the localization and grain size of the mineralogy (and organics if present) compared to SuperCam. Concerning the rock types we investigated, this spatial resolution would have likely enabled us to separate the individual contributions of the various phases present which have grain sizes typically above 20 µm. This is typically the case for MicrOmega, as described in [67]. However, since both techniques (Raman and VISIR) can yield non-linear response when mixtures are present, and since some phases are not, or are only weakly IR or Raman active (ex: sulfides, opaques, glasses), the presence of LIBS would help build a more quantitative picture of the sample, and assess the presence of some trace elements to which IR and Raman are insensitive. In the framework of a small rover platform or helicopter-based exploration of Mars, a micro-LIBS instrument is currently being developed [78] with intended spatial resolution of 50  $\mu$ m, and the capability to perform scans of 30  $\times$  30 points, on a 5  $\times$  5 mm area. This spatial resolution may help extract the mineralogical endmembers, which was not possible in our work based on current LIBS instrumentation on Mars. However, to do so, a very accurate calibration of elemental abundances may be needed to look at the alteration of ultramafic rock since for instance (Fe+Mg)/Si ratio are very close between olivine and serpentine. Alternatively, if the H abundance shows clear grain boundaries, that could also aid in distinguishing between olivine and secondary phases.

# CRediT authorship contribution statement

C. Collet: Writing – review & editing, Writing – original draft, Methodology, Formal analysis. A. Cousin: Writing – review & editing, Methodology, Investigation, Funding acquisition, Formal analysis, Conceptualization. O. Beyssac: Writing – review & editing, Validation, Supervision, Methodology, Conceptualization. P. Beck: Writing – review & editing, Validation, Supervision. O. Forni: Validation, Software. S. Clegg: Formal analysis. J. Comellas: Validation, Conceptualization. E. Clavé: Writing – review & editing. A. Fau: Software, Data curation. S. Pont: Software. F. Poulet: Validation. R.K. Martinez: Software. H. Austrheim: Resources. S. Maurice: Validation. R.C. Wiens: Writing – review & editing, Validation.

# Declaration of competing interest

The authors declare that they have no known competing financial interests or personal relationships that could have appeared to influence the work reported in this paper.

## Acknowledgments

The authors would like to thank P. Pinet, Yves Daydou and Sebastien Fabre from IRAP for their expertise and fruitful discussion on this thematic. NASA contract NNH13ZDA018O to LANL and Purdue. This project is conducted in France under the authority of CNES.

# Appendix A. Supplementary data

Supplementary material related to this article can be found online at https://doi.org/10.1016/j.sab.2025.107338.

#### Data availability

Data will be made available on request.

#### References

- [1] K.A. Farley, K.H. Williford, K.M. Stack, R. Bhartia, A. Chen, M. de la Torre, K. Hand, Y. Goreva, C.D.K. Herd, R. Hueso, Y. Liu, J.N. Maki, G. Martinez, R.C. Moeller, A. Nelessen, C.E. Newman, D. Nunes, A. Ponce, N. Spanovich, P.A. Willis, L.W. Beegle, J.F. Bell, A.J. Brown, S.-E. Hamran, J.A. Hurowitz, S. Maurice, D.A. Paige, J.A. Rodriguez-Manfredi, M. Schulte, R.C. Wiens, Mars 2020 mission overview, Space Sci. Rev. 216 (8) (2020) http://dx.doi.org/10.1007/s11214-020-00762-y.
- [2] K.M. Stack, N.R. Williams, F. Calef, V.Z. Sun, K.H. Williford, K.A. Farley, S. Eide, D. Flannery, C. Hughes, S.R. Jacob, L.C. Kah, F. Meyen, A. Molina, C.Q. Nataf, M. Rice, P. Russell, E. Scheller, C.H. Seeger, W.J. Abbey, J.B. Adler, H. Amundsen, R.B. Anderson, S.M. Angel, G. Arana, J. Atkins, M. Barrington, T. Berger, R. Borden, B. Boring, A. Brown, B.L. Carrier, P. Conrad, H. Dypvik, S.A. Fagents, Z.E. Gallegos, B. Garczynski, K. Golder, F. Gomez, Y. Goreva, S. Gupta, S.-E. Hamran, T. Hicks, E.D. Hinterman, B.N. Horgan, J. Hurowitz, J.R. Johnson, J. Lasue, R.E. Kronyak, Y. Liu, J.M. Madariaga, N. Mangold, J. McClean, N. Miklusicak, D. Nunes, C. Rojas, K. Runyon, N. Schmitz, N. Scudder, E. Shaver, J. SooHoo, R. Spaulding, E. Stanish, L.K. Tamppari, M.M. Tice, N. Turenne, P.A. Willis, R. Aileen Yingst, Photogeologic map of the perseverance rover field site in Jezero Crater constructed by the mars 2020 science team, Space Sci. Rev. 216 (8) (2020) http://dx.doi.org/10.1007/s11214-020-00739-x.
- [3] T.A. Goudge, K.L. Aureli, J.W. Head, C.I. Fassett, J.F. Mustard, Classification and analysis of candidate impact crater-hosted closed-basin lakes on mars, Icarus 260 (2015) 346–367, http://dx.doi.org/10.1016/j.icarus.2015.07.026.
- [4] B.H. Horgan, R.B. Anderson, G. Dromart, E.S. Amador, M.S. Rice, The mineral diversity of jezero crater: Evidence for possible lacustrine carbonates on mars, Icarus 339 (2020) 113526, http://dx.doi.org/10.1016/j.icarus.2019.113526.
- [5] B.L. Ehlmann, J.F. Mustard, G.A. Swayze, R.N. Clark, J.L. Bishop, F. Poulet, D.J. Des Marais, L.H. Roach, R.E. Milliken, J.J. Wray, O. Barnouin-Jha, S.L. Murchie, Identification of hydrated silicate minerals on mars using MRO-CRISM: Geologic context near nili fossae and implications for aqueous alteration, J. Geophys. Res.: Planets 114 (E2) (2009) http://dx.doi.org/10.1029/2009je003339.
- [6] T.M. Hoefen, R.N. Clark, J.L. Bandfield, M.D. Smith, J.C. Pearl, P.R. Christensen, Discovery of olivine in the Nili Fossae Region of mars, Science 302 (5645) (2003) 627–630, http://dx.doi.org/10.1126/science.1089647.
- [7] L. Mandon, C. Quantin-Nataf, P. Thollot, N. Mangold, L. Lozac'h, G. Dromart, P. Beck, E. Dehouck, S. Breton, C. Millot, M. Volat, Refining the age, emplacement and alteration scenarios of the olivine-rich unit in the Nili Fossae region, mars, Icarus 336 (2020) 113436, http://dx.doi.org/10.1016/j.icarus.2019.113436.
- [8] J.F. Mustard, F. Poulet, A. Gendrin, J.-P. Bibring, Y. Langevin, B. Gondet, N. Mangold, G. Bellucci, F. Altieri, Olivine and pyroxene diversity in the crust of mars, Science 307 (5715) (2005) 1594–1597, http://dx.doi.org/10.1126/science. 1109098.
- [9] A.J. Brown, C.E. Viviano, T.A. Goudge, Olivine-carbonate mineralogy of the Jezero Crater Region, J. Geophys. Res.: Planets 125 (3) (2020) http://dx.doi. org/10.1029/2019je006011.
- [10] B.L. Ehlmann, J.F. Mustard, S.L. Murchie, F. Poulet, J.L. Bishop, A.J. Brown, W.M. Calvin, R.N. Clark, D.J.D. Marais, R.E. Milliken, L.H. Roach, T.L. Roush, G.A. Swayze, J.J. Wray, Orbital identification of carbonate-bearing rocks on mars, Science 322 (5909) (2008) 1828–1832, http://dx.doi.org/10.1126/science. 1164759
- [11] A.J. Brown, S.J. Hook, A.M. Baldridge, J.K. Crowley, N.T. Bridges, B.J. Thomson, G.M. Marion, C.R. de Souza Filho, J.L. Bishop, Hydrothermal formation of clay-carbonate alteration assemblages in the Nili Fossae region of mars, Earth Planet. Sci. Lett. 297 (1–2) (2010) 174–182, http://dx.doi.org/10.1016/j.epsl.2010.06.

- [12] C.E. Viviano, J.E. Moersch, H.Y. McSween, Implications for early hydrothermal environments on mars through the spectral evidence for carbonation and chloritization reactions in the Nili Fossae region, J. Geophys. Res.: Planets 118 (9) (2013) 1858–1872, http://dx.doi.org/10.1002/jgre.20141.
- [13] R.C. Wiens, S. Maurice, S.H. Robinson, A.E. Nelson, P. Cais, P. Bernardi, R.T. Newell, S. Clegg, S.K. Sharma, S. Storms, J. Deming, D. Beckman, A.M. Ollila, O. Gasnault, R.B. Anderson, Y. André, S.M. Angel, G. Arana, E. Auden, P. Beck, J. Becker, K. Benzerara, S. Bernard, O. Beyssac, L. Borges, B. Bousquet, K. Boyd, M. Caffrey, J. Carlson, K. Castro, J. Celis, B. Chide, K. Clark, E. Cloutis, E.C. Cordoba, A. Cousin, M. Dale, L. Deflores, D. Delapp, M. Deleuze, M. Dirmyer, C. Donny, G. Dromart, M.G. Duran, M. Egan, J. Ervin, C. Fabre, A. Fau, W. Fischer, O. Forni, T. Fouchet, R. Fresquez, J. Frydenvang, D. Gasway, I. Gontijo, J. Grotzinger, X. Jacob, S. Jacquinod, J.R. Johnson, R.A. Klisiewicz, J. Lake, N. Lanza, J. Laserna, J. Lasue, S.L. Mouélic, C. Legett, R. Leveille, E. Lewin, G. Lopez-Reyes, R. Lorenz, E. Lorigny, S.P. Love, B. Lucero, J.M. Madariaga, M. Madsen, S. Madsen, N. Mangold, J.A. Manrique, J.P. Martinez, J. Martinez-Frias, K.P. McCabe, T.H. McConnochie, J.M. McGlown, S.M. McLennan, N. Melikechi, P.-Y. Meslin, J.M. Michel, D. Mimoun, A. Misra, G. Montagnac, F. Montmessin, V. Mousset, N. Murdoch, H. Newsom, L.A. Ott, Z.R. Ousnamer, L. Pares, Y. Parot, R. Pawluczyk, C.G. Peterson, P. Pilleri, P. Pinet, G. Pont, F. Poulet, C. Provost, B. Quertier, H. Quinn, W. Rapin, J.-M. Reess, A.H. Regan, A.L. Reyes-Newell, P.J. Romano, C. Royer, F. Rull, B. Sandoval, J.H. Sarrao, V. Sautter, M.J. Schoppers, S. Schröder, D. Seitz, T. Shepherd, P. Sobron, B. Dubois, V. Sridhar, M.J. Toplis, I. Torre-Fdez, I.A. Trettel, M. Underwood, A. Valdez, J. Valdez, D. Venhaus, P. Willis, The SuperCam instrument suite on the NASA mars 2020 rover: Body unit and combined system tests, Space Sci. Rev. 217 (1) (2020) http://dx.doi.org/10.1007/s11214-020-00777-5.
- [14] S. Maurice, R.C. Wiens, P. Bernardi, P. Caïs, S. Robinson, T. Nelson, O. Gasnault, J.-M. Reess, M. Deleuze, F. Rull, J.-A. Manrique, S. Abbaki, R.B. Anderson, Y. André, S.M. Angel, G. Arana, T. Battault, P. Beck, K. Benzerara, S. Bernard, J.-P. Berthias, O. Beyssac, M. Bonafous, B. Bousquet, M. Boutillier, A. Cadu, K. Castro, F. Chapron, B. Chide, K. Clark, E. Clavé, S. Clegg, E. Cloutis, C. Collin, E.C. Cordoba, A. Cousin, J.-C. Dameury, W. D'Anna, Y. Daydou, A. Debus, L. Deflores, E. Dehouck, D. Delapp, G.D.L. Santos, C. Donny, A. Doressoundiram, G. Dromart, B. Dubois, A. Dufour, M. Dupieux, M. Egan, J. Ervin, C. Fabre, A. Fau, W. Fischer, O. Forni, T. Fouchet, J. Frydenvang, S. Gauffre, M. Gauthier, V. Gharakanian, O. Gilard, I. Gontijo, R. Gonzalez, D. Granena, J. Grotzinger, R. Hassen-Khodja, M. Heim, Y. Hello, G. Hervet, O. Humeau, X. Jacob, S. Jacquinod, J.R. Johnson, D. Kouach, G. Lacombe, N. Lanza, L. Lapauw, J. Laserna, J. Lasue, L.L. Deit, S.L. Mouélic, E.L. Comte, Q.-M. Lee, C. Legett, R. Leveille, E. Lewin, C. Levrat, G. Lopez-Reves, R. Lorenz, B. Lucero, J.M. Madariaga, S. Madsen, M. Madsen, N. Mangold, F. Manni, J.-F. Mariscal, J. Martinez-Frias, K. Mathieu, R. Mathon, K.P. McCabe, T. McConnochie, S.M. McLennan, J. Mekki, N. Melikechi, P.-Y. Meslin, Y. Micheau, Y. Michel, J.M. Michel, D. Mimoun, A. Misra, G. Montagnac, C. Montaron, F. Montmessin, J. Moros, V. Mousset, Y. Morizet, N. Murdoch, R.T. Newell, H. Newsom, N.N. Tuong, A.M. Ollila, G. Orttner, L. Oudda, L. Pares, J. Parisot, Y. Parot, R. Pérez, D. Pheav, L. Picot, P. Pilleri, C. Pilorget, P. Pinet, G. Pont, F. Poulet, C. Quantin-Nataf, B. Quertier, D. Rambaud, W. Rapin, P. Romano, L. Roucayrol, C. Royer, M. Ruellan, B.F. Sandoval, V. Sautter, M.J. Schoppers, S. Schröder, H.-C. Seran, S.K. Sharma, P. Sobron, M. Sodki, A. Sournac, V. Sridhar, D. Standarovsky, S. Storms, N. Striebig, M. Tatat, M. Toplis, I. Torre-Fdez, N. Toulemont, C. Velasco, M. Veneranda, D. Venhaus, C. Virmontois, M. Viso, P. Willis, K.W. Wong, The SuperCam instrument suite on the mars 2020 rover; Science objectives and mast-unit description, Space Sci. Rev. 217 (3) (2021) http://dx.doi.org/10.1007/s11214-021-00807-w.
- [15] T. Fouchet, J.-M. Reess, F. Montmessin, R. Hassen-Khodja, N. Nguyen-Tuong, O. Humeau, S. Jacquinod, L. Lapauw, J. Parisot, M. Bonafous, P. Bernardi, F. Chapron, A. Jeanneau, C. Collin, D. Zeganadin, P. Nibert, S. Abbaki, C. Montaron, C. Blanchard, V. Arslanyan, O. Achelhi, C. Colon, C. Royer, V. Hamm, M. Beuzit, F. Poulet, C. Pilorget, L. Mandon, O. Forni, A. Cousin, O. Gasnault, P. Pilleri, B. Dubois, C. Quantin, P. Beck, O. Beyssac, S. Le Mouélic, J.R. Johnsson, T.H. McConnochie, S. Maurice, R.C. Wiens, The SuperCam infrared spectrometer for the perseverance rover of the mars2020 mission, Icarus 373 (2022) 114773, http://dx.doi.org/10.1016/j.icarus.2021.114773.
- [16] K.A. Farley, K.M. Stack, D.L. Shuster, B.H.N. Horgan, J.A. Hurowitz, J.D. Tarnas, J.I. Simon, V.Z. Sun, E.L. Scheller, K.R. Moore, S.M. McLennan, P.M. Vasconcelos, R.C. Wiens, A.H. Treiman, L.E. Mayhew, O. Beyssac, T.V. Kizovski, N.J. Tosca, K.H. Williford, L.S. Crumpler, L.W. Beegle, J.F. Bell, B.L. Ehlmann, Y. Liu, J.N. Maki, M.E. Schmidt, A.C. Allwood, H.E.F. Amundsen, R. Bhartia, T. Bosak, A.J. Brown, B.C. Clark, A. Cousin, O. Forni, T.S.J. Gabriel, Y. Goreva, S. Gupta, S.-E. Hamran, C.D.K. Herd, K. Hickman-Lewis, J.R. Johnson, L.C. Kah, P.B. Kelemen, K.B. Kinch, L. Mandon, N. Mangold, C. Quantin-Nataf, M.S. Rice, P.S. Russell, S. Sharma, S. Siljeström, A. Steele, R. Sullivan, M. Wadhwa, B.P. Weiss, A.J. Williams, B.V. Wogsland, P.A. Willis, T.A. Acosta-Maeda, P. Beck, K. Benzerara, S. Bernard, A.S. Burton, E.L. Cardarelli, B. Chide, E. Clavé, E.A. Cloutis, B.A. Cohen, A.D. Czaja, V. Debaille, E. Dehouck, A.G. Fairén, D.T. Flannery, S.Z. Fleron, T. Fouchet, J. Frydenvang, B.J. Garczynski, E.F. Gibbons, E.M. Hausrath, A.G. Hayes, J. Henneke, J.L. Jørgensen, E.M. Kelly, J. Lasue, S.L. Mouélic, J.M. Madariaga, S. Maurice, M. Merusi, P.-Y. Meslin, S.M. Milkovich, C.C. Million, R.C. Moeller, J.I.N. nez, A.M. Ollila, G. Paar, D.A. Paige, D.A.K. Pedersen, P.

- Pilleri, C. Pilorget, P.C. Pinet, J.W. Rice, C. Royer, V. Sautter, M. Schulte, M.A. Sephton, S.K. Sharma, S.F. Sholes, N. Spanovich, M.S. Clair, C.D. Tate, K. Uckert, S.J. VanBommel, A.G. Yanchillina, M.-P. Zorzano, Aqueously altered igneous rocks sampled on the floor of jezero crater, mars, Science 377 (6614) (2022) http://dx.doi.org/10.1126/science.abo2196.
- [17] R.C. Wiens, A. Udry, O. Beyssac, C. Quantin-Nataf, N. Mangold, A. Cousin, L. Mandon, T. Bosak, O. Forni, S.M. McLennan, V. Sautter, A. Brown, K. Benzerara, J.R. Johnson, L. Mayhew, S. Maurice, R.B. Anderson, S.M. Clegg, L. Crumpler, T.S.J. Gabriel, P. Gasda, J. Hall, B.H.N. Horgan, L. Kah, C. Legett, J.M. Madariaga, P.-Y. Meslin, A.M. Ollila, F. Poulet, C. Royer, S.K. Sharma, S. Siljeström, J.I. Simon, T.E. Acosta-Maeda, C. Alvarez-Llamas, S.M. Angel, G. Arana, P. Beck, S. Bernard, T. Bertrand, B. Bousquet, K. Castro, B. Chide, E. Clavé E Cloutis S Connell E Dehouck G Dromart W Fischer T Fouchet R. Francis, J. Frydenvang, O. Gasnault, E. Gibbons, S. Gupta, E.M. Hausrath, X. Jacob, H. Kalucha, E. Kelly, E. Knutsen, N. Lanza, J. Laserna, J. Lasue, S. Le Mouélic, R. Leveille, G. Lopez Reyes, R. Lorenz, J.A. Manrique, J. Martinez-Frias, T. McConnochie, N. Melikechi, D. Mimoun, F. Montmessin, J. Moros, N. Murdoch, P. Pilleri, C. Pilorget, P. Pinet, W. Rapin, F. Rull, S. Schröder, D.L. Shuster, R.J. Smith, A.E. Stott, J. Tarnas, N. Turenne, M. Veneranda, D.S. Vogt, B.P. Weiss, P. Willis, K.M. Stack, K.H. Williford, K.A. Farley, Compositionally and density stratified igneous terrain in Jezero crater, mars, Sci. Adv. 8 (34) (2022) http://dx.doi.org/10.1126/sciadv.abo3399.
- [18] Y. Liu, M.M. Tice, M.E. Schmidt, A.H. Treiman, T.V. Kizovski, J.A. Hurowitz, A.C. Allwood, J. Henneke, D.A.K. Pedersen, S.J. VanBommel, M.W.M. Jones, A.L. Knight, B.J. Orenstein, B.C. Clark, W.T. Elam, C.M. Heirwegh, T. Barber, L.W. Beegle, K. Benzerara, S. Bernard, O. Beyssac, T. Bosak, A.J. Brown, E.L. Cardarelli, D.C. Catling, J.R. Christian, E.A. Cloutis, B.A. Cohen, S. Davidoff, A.G. Fairén, K.A. Farley, D.T. Flannery, A. Galvin, J.P. Grotzinger, S. Gupta, J. Hall, C.D.K. Herd, K. Hickman-Lewis, R.P. Hodyss, B.H.N. Horgan, J.R. Johnson, J.L. Jørgensen, L.C. Kah, J.N. Maki, L. Mandon, N. Mangold, F.M. McCubbin, S.M. McLennan, K. Moore, M. Nachon, P. Nemere, L.D. Nothdurft, J.I. Núñez, L. O'Neil, C.M. Quantin-Nataf, V. Sautter, D.L. Shuster, K.L. Siebach, J.I. Simon, K.P. Sinclair, K.M. Stack, A. Steele, J.D. Tarnas, N.J. Tosca, K. Uckert, A. Udry, L.A. Wade, B.P. Weiss, R.C. Wiens, K.H. Williford, M.-P. Zorzano, An olivine cumulate outcrop on the floor of jezero crater, mars, Science 377 (6614) (2022) 1513–1519, http://dx.doi.org/10.1126/science.abo2756.
- [19] A. Udry, A. Ostwald, V. Sautter, A. Cousin, O. Beyssac, O. Forni, G. Dromart, K. Benzerara, M. Nachon, B. Horgan, L. Mandon, E. Clavé, E. Dehouck, E. Gibbons, S. Alwmark, E. Ravanis, R.C. Wiens, C. Legett, R. Anderson, P. Pilleri, N. Mangold, M. Schmidt, Y. Liu, J.I. Núñez, K. Castro, J.M. Madariaga, T. Kizovski, P. Beck, S. Bernard, T. Bosak, A. Brown, S. Clegg, E. Cloutis, B. Cohen, S. Connell, L. Crumpler, V. Debaille, D. Flannery, T. Fouchet, T.S.J. Gabriel, O. Gasnault, C.D.K. Herd, J. Johnson, J.A. Manrique, S. Maurice, F.M. McCubbin, S. McLennan, A. Ollila, P. Pinet, C. Quantin-Nataf, C. Royer, S. Sharma, J.I. Simon, A. Steele, N. Tosca, A. Treiman, A mars 2020 perseverance SuperCam perspective on the igneous nature of the máaz formation at jezero crater and link with séítah, mars, J. Geophys. Res.: Planets 128 (7) (2023) http://dx.doi.org/10.1029/2022je007440.
- [20] O. Beyssac, O. Forni, A. Cousin, A. Udry, L.C. Kah, L. Mandon, O.E. Clavé, Y. Liu, F. Poulet, C.Q. Nataf, O. Gasnault, J.R. Johnson, K. Benzerara, P. Beck, E. Dehouck, N. Mangold, C.A. Llamas, R.B. Anderson, G. Arana, R. Barnes, S. Bernard, T. Bosak, A.J. Brown, K. Castro, B. Chide, S.M. Clegg, E. Cloutis, T. Fouchet, T. Gabriel, S. Gupta, G. Lacombe, J. Lasue, S.L. Mouelic, G. Lopez-Reyes, J.M. Madariaga, F.M. McCubbin, S.M. McLennan, J.A. Manrique, P.Y. Meslin, F. Montmessin, J.N. nez, A.M. Ollila, A. Ostwald, P. Pilleri, P. Pinet, C. Royer, S.K. Sharma, S. Schröder, J.I. Simon, M.J. Toplis, M. Veneranda, P.A. Willis, S. Maurice, R.C.W. and, Petrological traverse of the olivine cumulate séítah formation at jezero crater, mars: A perspective from SuperCam onboard perseverance, J. Geophys. Res.: Planets 128 (7) (2023) http://dx.doi.org/10.1029/2022je007638.
- [21] E. Clavé, K. Benzerara, P.-Y. Meslin, O. Forni, C. Royer, L. Mandon, P. Beck, C. Quantin-Nataf, O. Beyssac, A. Cousin, B. Bousquet, R.C. Wiens, S. Maurice, E. Dehouck, S. Schröder, O. Gasnault, N. Mangold, G. Dromart, T. Bosak, S. Bernard, A. Udry, R.B. Anderson, G. Arana, A.J. Brown, K. Castro, S.M. Clegg, E. Cloutis, A.G. Fairén, D.T. Flannery, P.J. Gasda, J.R. Johnson, J. Lasue, G. Lopez-Reyes, J.M. Madariaga, J.A. Manrique, S. Le Mouélic, J.I. Núñez, A.M. Ollila, P. Pilleri, C. Pilorget, P. Pinet, F. Poulet, M. Veneranda, Z.U. Wolf, Carbonate detection with SuperCam in igneous rocks on the floor of jezero crater, mars, J. Geophys. Res.: Planets 128 (6) (2023) http://dx.doi.org/10.1029/2022je007463.
- [22] P.-Y. Meslin, O. Forni, P. Beck, A. Cousin, O. Beyssac, G. Lopez-Reyes, K. Benzerara, A. Ollila, L. Mandon, R.C. Wiens, S. Clegg, G. Montagnac, E. Clavé, J.-A. Manrique, B. Chide, S. Maurice, O. Gasnault, J. Lasue, C. Quantin-Nataf, E. Dehouck, S.K. Sharma, G. Arana, J.M. Madariaga, K. Castro, S. Schröder, N. Mangold, F. Poulet, J. Johnson, S. Le Mouélic, M.-P. Zorzano, Evidence for perchlorate and sulfate salts in jezero crater, mars, from supercam observations, in: Lunar and Planetary Science Conference, in: Lunar and Planetary Science Conference, vol. 53, Lunar and Planetary Institute, The Woodlands, TX, United States, 2022, p. 2694, URL https://hal.science/hal-03849351.
- [23] M.M. Tice, J.A. Hurowitz, A.C. Allwood, M.W.M. Jones, B.J. Orenstein, S. Davidoff, A.P. Wright, D.A. Pedersen, J. Henneke, N.J. Tosca, K.R. Moore, B.C.

- Clark, S.M. McLennan, D.T. Flannery, A. Steele, A.J. Brown, M.-P. Zorzano, K. Hickman-Lewis, Y. Liu, S.J. VanBommel, M.E. Schmidt, T.V. Kizovski, A.H. Treiman, L. O'Neil, A.G. Fairén, D.L. Shuster, S. Gupta, T.P. Team, Alteration history of séítah formation rocks inferred by PIXL x-ray fluorescence, x-ray diffraction, and multispectral imaging on mars, Sci. Adv. 8 (47) (2022) eabp9084, http://dx.doi.org/10.1126/sciadv.abp9084.
- [24] M.E. Schmidt, T.V. Kizovski, Y. Liu, J.D. Hernandez-Montenegro, M.M. Tice, A.H. Treiman, J.A. Hurowitz, D.A. Klevang, A.L. Knight, J. Labrie, N.J. Tosca, S.J. VanBommel, S. Benaroya, L.S. Crumpler, B.H.N. Horgan, R.V. Morris, J.I. Simon, A. Udry, A. Yanchilina, A.C. Allwood, M.L. Cable, J.R. Christian, B.C. Clark, D.T. Flannery, C.M. Heirwegh, T.L.J. Henley, J. Henneke, M.W.M. Jones, B.J. Orenstein, C.D.K. Herd, N. Randazzo, D. Shuster, M. Wadhwa, Diverse and highly differentiated lava suite in jezero crater, mars: Constraints on intracrustal magmatism revealed by mars 2020 PIXL, Sci. Adv. 11 (4) (2025) eadr2613, http://dx.doi.org/10.1126/sciadv.adr2613.
- [25] N. Tosca, M. Tice, J. Hurowitz, D. Pedersen, J. Henneke, L. Mandon, F. McCubbin, O. Ross, P. Tung, R. Harrison, A. Li, M. Schmidt, T. Kizovski, Y. Liu, L. Mayhew, M. Jones, J. Labrie, S. Davidoff, A. Allwood, O. Beyssac, A. Brown, M. Cable, J. Comellas, B. Clark, A. Galvin, B. Horgan, C. Heirwegh, P. Nemere, B. Orenstein, C. Quantin-Nataf, C. Royer, A. Treiman, L. Wade, R. Wiens, A. Wright, In situ evidence for serpentinization within the máaz formation, jezero crater, mars, 2025, http://dx.doi.org/10.17863/CAM.118334.
- [26] E. Moreland, K. Siebach, G. Costin, Y. Jiang, M. Tice, J. Hurowitz, A. Treiman, J. Simon, Y. Liu, A. Udry, et al., Identifying stoichiometric minerals in PIXL data from the first three years of the mars 2020 mission using the MIST algorithm, in: International Conference on Mars, vol. 3007, 2024, p. 3161.
- [27] L. Mandon, C. Quantin-Nataf, C. Royer, P. Beck, T. Fouchet, J.R. Johnson, E. Dehouck, S. Le Mouélic, F. Poulet, F. Montmessin, C. Pilorget, O. Gasnault, O. Forni, L.E. Mayhew, O. Beyssac, T. Bertrand, E. Clavé, P. Pinet, A.J. Brown, C. Legett, J. Tarnas, E.A. Cloutis, G. Poggiali, T. Fornaro, S. Maurice, R.C. Wiens, Reflectance of jezero crater floor: 2. Mineralogical interpretation, J. Geophys. Res.: Planets 128 (7) (2023) http://dx.doi.org/10.1029/2022je007450.
- [28] E. Dehouck, O. Forni, C. Quantin-Nataf, P. Beck, N. Mangold, C. Royer, E. Clavé, O. Beyssac, J. Johnson, L. Mandon, F. Poulet, S. Le Mouélic, G. Caravaca, H. Kalucha, E. Gibbons, G. Dromart, P. Gasda, P.-Y. Meslin, A. Williams, S. Schroeder, A. Udry, R. Anderson, S. Clegg, A. Cousin, T. Gabriel, J. Lasue, T. Fouchet, P. Pilleri, C. Pilorget, J. Hurowitz, J. Núñez, P. Russell, J. Simon, S. Maurice, R. Wiens, Geochemistry and mineralogy of ancient sedimentary rocks analyzed by the SuperCam instrument in the Jezero Delta, mars, in: Goldschmidt2023 Abstracts, European Association of Geochemistry, 2023, http://dx.doi.org/10.7185/gold2023.18636.
- [29] J.A. Hurowitz, M.M. Tice, A.C. Allwood, M.L. Cable, T. Bosak, A. Broz, G. Caravaca, B.C. Clark, E. Dehouck, A.G. Fairén, et al., The petrogenetic history of the jezero crater delta front from microscale observations by the mars 2020 PIXL instrument, in: 54th Lunar and Planetary Science Conference 2023, vol. 54, 2023.
- [30] B. Horgan, B. Garczynski, S. Gupta, A. Jones, R. Barnes, J. Hurowitz, M. Tice, E.L. Cardarelli, P.S. Russell, R. Wiens, S. Siljeström, K. Stack, S. Sholes, J.F. Bell, J.R. Johnson, J. Núñez, N. Randazzo, J.I. Simon, Mars 2020 Science Team, Campaign Overview and Initial Results from Exploration of the Margin Unit in Jezero Crater by the Perseverance Rover, in: 55th Lunar and Planetary Science Conference, in: LPI Contributions, vol. 3040, 2024, p. 2624.
- [31] E. Clavé, P. Beck, O. Beyssac, O. Forni, S. Schröder, N. Mangold, C. Royer, L. Mandon, E. Dehouck, S. Le Mouélic, et al., Carbonation of mafic rocks in the margin unit, jezero crater, MARS, in: International Conference on Mars, vol. 3007, 2024, p. 3161.
- [32] E.L. Moreland, K.L. Siebach, J. Hurowitz, C.C. Bedford, A.H. Treiman, Stoichiometric Mineral identifications And uncertainties From sols 900–1400 Of The Mars 2020 Mission With pixl And Mist, in: 56th Lunar and Planetary Science Conference, LPSC, 2025.
- [33] L. Mayhew, E. Ravanis, C. Quantin-Nataf, K.M. Stack, K. Farley, C. Herd, et al., STRATEGIC APPROACH AND FIRST RESULTS FROM THE JEZERO crater rim campaign., in: 56th Lunar and Planetary Science Conference, LPSC, 2025.
- [34] C. Quantin-Nataf, E. Dehouck, P. Beck, C. Bedford, L. Mandon, O. Beyssac, E. Clavé, et al., Alteration diversity observed in the inner part of Jezero Crater Rim, in: 56th Lunar and Planetary Science Conference, LPSC, 2025.
- [35] C. Bedford, R. Wiens, B. Horgan, A. Klidaras, C. Quantin-Nataf, A. Udry, S. Alwmark, C. Herd, E. Ravanis, A. Treiman, et al., Geological diversity in the jezero crater rim investigated with supercam: Insights into impact processes on mars, in: 56th Lunar and Planetary Science Conference, LPSC, 2025.
- [36] E. Ravanis, B. Horgan, A. Vaughan, B. Garczynski, J. Johnson, A. Klidaras, M. Deahn, M. Rice, C. Bedford, et al., Diverse igneoUs Rocks Observed During The Mars2020 Crater Rim campaign In Jezero crater Using Mastcam-z multispectral data., in: 56th Lunar and Planetary Science Conference, LPSC, 2025.
- [37] K. Uckert, C. Lee, L. Kah, R. Williams, A. Murphy, M. Minitti, S. Siljeström, R. Bhartia, A. Yingst, et al., Jezero crater Rim: Initial Textural observations And compositional Analyses From the Sherloc Deep Uv Raman And fluorescence spectrometer, in: 56th Lunar and Planetary Science Conference, LPSC, 2025.
- [38] B.W. Evans, The serpentinite multisystem revisited: Chrysotile is metastable, Int. Geol. Rev. 46 (6) (2004) 479–506, http://dx.doi.org/10.2747/0020-6814.46.6. 479

- [39] L. Mandon, B.L. Ehlmann, R.N. Greenberger, E.T. Ellison, L.E. Mayhew, A.S. Templeton, Hyperspectral mapping of a kilometer of mantle rock core: insight into active serpentinization systems, in: EGU General Assembly Conference Abstracts, in: EGU General Assembly Conference Abstracts, in: EGU General Assembly Conference Abstracts, 2024, p. 4012, http://dx.doi.org/10.5194/egusphere-egu24-4012.
- [40] A. Beinlich, H. Austrheim, J. Glodny, M. Erambert, T.B. Andersen, CO2 sequestration and extreme Mg depletion in serpentinized peridotite clasts from the devonian solund basin, SW-Norway, Geochim. Cosmochim. Acta 74 (24) (2010) 6935–6964, http://dx.doi.org/10.1016/j.gca.2010.07.027.
- [41] A. Beinlich, V. Mavromatis, H. Austrheim, E.H. Oelkers, Inter-mineral Mg isotope fractionation during hydrothermal ultramafic rock alteration-implications for the global Mg-cycle, Earth Planet. Sci. Lett. 392 (2014) 166–176, http://dx.doi.org/ 10.1016/j.epsl.2014.02.028.
- [42] O. Ulven, A. Beinlich, J. Hövelmann, H. Austrheim, B. Jamtveit, Subarctic physicochemical weathering of serpentinized peridotite, Earth Planet. Sci. Lett. 468 (2017) 11–26, http://dx.doi.org/10.1016/j.epsl.2017.03.030.
- [43] A. Fau, O. Beyssac, M. Gauthier, P. Meslin, A. Cousin, K. Benzerara, S. Bernard, J. Boulliard, O. Gasnault, O. Forni, R. Wiens, M. Morand, P. Rosier, Y. Garino, S. Pont, S. Maurice, Pulsed laser-induced heating of mineral phases: Implications for laser-induced breakdown spectroscopy combined with Raman spectroscopy, Spectrochim. Acta Part B: At. Spectrosc. 160 (2019) 105687, http://dx.doi.org/10.1016/j.sab.2019.105687.
- [44] S. Bernard, O. Beyssac, K. Benzerara, Raman mapping using advanced linescanning systems: Geological applications, Appl. Spectrosc. 62 (11) (2008) 1180–1188, http://dx.doi.org/10.1366/000370208786401581.
- [45] O. Beyssac, New trends in Raman spectroscopy: From high-resolution geochemistry to planetary exploration, Elements 16 (2) (2020) 117–122, http://dx.doi.org/10.2138/gselements.16.2.117.
- [46] A. Fau, O. Beyssac, M. Gauthier, G. Panczer, O. Gasnault, P.-Y. Meslin, S. Bernard, S. Maurice, O. Forni, J.-C. Boulliard, F. Bosc, C. Drouet, Time-resolved Raman and luminescence spectroscopy of synthetic REE-doped hydroxylapatites and natural apatites, Am. Mineral. 107 (7) (2022) 1341–1352, http://dx.doi.org/10.2138/am-2022-8006.
- [47] C. Royer, S. Bernard, O. Beyssac, E. Balan, O. Forni, M. Gauthier, M. Morand, Y. Garino, P. Rosier, Impact of UV radiation on the Raman and infrared spectral signatures of sulfates, phosphates and carbonates: Implications for mars exploration, Icarus 410 (2024) 115894, http://dx.doi.org/10.1016/j.icarus.2023. 115804
- [48] K.E. Kuebler, B.L. Jolliff, A. Wang, L.A. Haskin, Extracting olivine (Fo-Fa) compositions from Raman spectral peak positions, Geochim. Cosmochim. Acta 70 (24) (2006) 6201–6222, http://dx.doi.org/10.1016/j.gca.2006.07.035.
- [49] R.B. Anderson, O. Forni, A. Cousin, R.C. Wiens, S.M. Clegg, J. Frydenvang, T.S. Gabriel, A. Ollila, S. Schröder, O. Beyssac, E. Gibbons, D.S. Vogt, E. Clavé, J.-A. Manrique, C. Legett, P. Pilleri, R.T. Newell, J. Sarrao, S. Maurice, G. Arana, K. Benzerara, P. Bernardi, S. Bernard, B. Bousquet, A.J. Brown, C. Alvarez-Llamas, B. Chide, E. Cloutis, J. Comellas, S. Connell, E. Dehouck, D.M. Delapp, A. Essunfeld, C. Fabre, T. Fouchet, C. Garcia-Florentino, L. García-Gómez, P. Gasda, O. Gasnault, E.M. Hausrath, N.L. Lanza, J. Laserna, J. Lasue, G. Lopez, J.M. Madariaga, L. Mandon, N. Mangold, P.-Y. Meslin, A.E. Nelson, H. Newsom, A.L. Reyes-Newell, S. Robinson, F. Rull, S. Sharma, J.I. Simon, P. Sobron, I.T. Fernandez, A. Udry, D. Venhaus, S.M. McLennan, R.V. Morris, B. Ehlmann, Postlanding major element quantification using SuperCam laser induced breakdown spectroscopy, Spectrochim. Acta Part B: At. Spectrosc. 188 (2022) 106347, http://dx.doi.org/10.1016/j.sab.2021.106347.
- [50] T.S.J. Gabriel, R.B. Anderson, R. Wiens, Dynamic Uncertainty Estimation of LIBS Chemistry on Mars with Gaussian Process Regression, in: 54th Lunar and Planetary Science Conference, in: LPI Contributions, vol. 2806, 2023, p. 2189.
- [51] D.A. Cremers, L.J. Radziemski, History and fundamentals of LIBS, Laser Induc. Break. Spectrosc.: Fundam. Appl. 1 (2006) 1–39.
- [52] W.M. Philip E. Gill, M.H. Wright, Practical Optimization, Academic Press Limited, 1981.
- [53] C. Fabre, S. Maurice, A. Cousin, R. Wiens, O. Forni, V. Sautter, D. Guillaume, Onboard calibration igneous targets for the mars science laboratory curiosity rover and the chemistry camera laser induced breakdown spectroscopy instrument, Spectrochim. Acta Part B: At. Spectrosc. 66 (3–4) (2011) 280–289, http://dx.doi.org/10.1016/j.sab.2011.03.012.
- [54] W. Rapin, B. Bousquet, J. Lasue, P.-Y. Meslin, J.-L. Lacour, C. Fabre, R. Wiens, J. Frydenvang, E. Dehouck, S. Maurice, O. Gasnault, O. Forni, A. Cousin, Roughness effects on the hydrogen signal in laser-induced breakdown spectroscopy, Spectrochim. Acta Part B: At. Spectrosc. 137 (2017) 13–22, http://dx.doi.org/10.1016/j.sab.2017.09.003.
- [55] P. Beck, P. Meslin, A. Fau, O. Forni, O. Gasnault, J. Lasue, A. Cousin, S. Schröder, S. Maurice, W. Rapin, R. Wiens, A. Ollila, E. Dehouck, N. Mangold, B. Garcia, S. Schwartz, W. Goetz, N. Lanza, Detectability of carbon with ChemCam LIBS: Distinguishing sample from mars atmospheric carbon, and application to gale crater, Icarus 408 (2024) 115840, http://dx.doi.org/10.1016/j.icarus.2023.
- [56] C. Royer, T. Fouchet, L. Mandon, F. Montmessin, F. Poulet, O. Forni, J.R. Johnson, C. Legett, S. Le Mouélic, O. Gasnault, C. Quantin-Nataf, P. Beck, E. Dehouck, E. Clavé, A.M. Ollila, C. Pilorget, P. Bernardi, J.-M. Reess, P. Pilleri,

- A. Brown, R.T. Newell, E. Cloutis, S. Maurice, R.C. Wiens, Reflectance of jezero crater floor: 1. Data processing and calibration of the infrared spectrometer (IRS) on SuperCam, J. Geophys. Res.: Planets 128 (1) (2023) http://dx.doi.org/10.
- [57] J.R. Johnson, J. Bell, S. Bender, D. Blaney, E. Cloutis, L. DeFlores, B. Ehlmann, O. Gasnault, B. Gondet, K. Kinch, M. Lemmon, S. Le Mouélic, S. Maurice, M. Rice, R. Wiens, ChemCam passive reflectance spectroscopy of surface materials at the curiosity landing site, mars, Icarus 249 (2015) 74–92, http://dx.doi.org/ 10.1016/j.icarus.2014.02.028.
- [58] S. Potin, O. Brissaud, P. Beck, B. Schmitt, Y. Magnard, J.-J. Correia, P. Rabou, L. Jocou, SHADOWS: a spectro-gonio radiometer for bidirectional reflectance studies of dark meteorites and terrestrial analogs: design, calibrations, and performances on challenging surfaces, Appl. Opt. 57 (28) (2018) 8279, http: //dx.doi.org/10.1364/ao.57.008279.
- [59] C.E. Viviano, F.P. Seelos, S.L. Murchie, E.G. Kahn, K.D. Seelos, H.W. Taylor, K. Taylor, B.L. Ehlmann, S.M. Wiseman, J.F. Mustard, M.F. Morgan, Revised CRISM spectral parameters and summary products based on the currently detected mineral diversity on mars, J. Geophys. Res.: Planets 119 (6) (2014) 1403–1431, http://dx.doi.org/10.1002/2014JE004627.
- [60] C.E. Viviano-Beck, "Mro CRISM type spectra library", 2015, https://crismtype-spectra.rsl.wustl.edu, NASA Planetary Data System.
- [61] S.K. Sharma, A.K. Misra, P.G. Lucey, R.C. Lentz, A combined remote Raman and LIBS instrument for characterizing minerals with 532nm laser excitation, Spectrochim. Acta Part A: Mol. Biomol. Spectrosc. 73 (3) (2009) 468–476, http:// dx.doi.org/10.1016/j.saa.2008.08.005, Raman Spectroscopy Applied to the Earth Sciences - Sensu Latu.
- [62] K. Rammelkamp, S. Schröder, B.A. Lomax, E. Clavé, H.-W. Hübers, LIBS for prospecting and Raman spectroscopy for monitoring: two feasibility studies for supporting in-situ resource utilization, Front. Space Technol. 5 (2024) 1336548.
- [63] B. Horgan, J.F. Bell III, Widespread weathered glass on the surface of Mars, Geology 40 (5) (2012) 391–394, http://dx.doi.org/10.1130/G32755.1.
- [64] M.E. Minitti, C.M. Weitz, M.D. Lane, J.L. Bishop, Morphology, chemistry, and spectral properties of Hawaiian rock coatings and implications for Mars, J. Geophys. Res. (Planets) 112 (E5) (2007) E05015, http://dx.doi.org/10.1029/ 2006JE002839.
- [65] Y. Zhuang, H. Zhang, P. Ma, T. Jiang, Y. Yang, R.E. Milliken, W. Hsu, Visible and near-infrared reflectance spectra of igneous rocks and their powders, Icarus 391 (2023) 115346, http://dx.doi.org/10.1016/j.icarus.2022.115346.
- [66] J. Harloff, G. Arnold, Near-infrared reflectance spectroscopy of bulk analog materials for planetary crust, Planet. Space Sci. 49 (2) (2001) 191–211.
- [67] D. Loizeau, C. Pilorget, F. Poulet, C. Lantz, J.-P. Bibring, V. Hamm, C. Royer, H. Dypvik, A.M. Krzesińska, F. Rull, S.C. Werner, Planetary terrestrial analogues library project: 3. Characterization of samples with MicrOmega, Astrobiology 22 (3) (2022) 263–292, http://dx.doi.org/10.1089/ast.2020.2420.
- [68] R.C. Wiens, S. Maurice, M.S. Team, ChemCam: Chemostratigraphy by the first mars microprobe, Elements 11 (1) (2015) 33–38.
- [69] O. Forni, M. Gaft, M.J. Toplis, S.M. Clegg, S. Maurice, R.C. Wiens, N. Mangold, O. Gasnault, V. Sautter, S. Le Mouélic, et al., First detection of fluorine on mars: Implications for gale crater's geochemistry, Geophys. Res. Lett. 42 (4) (2015) 1020–1028.
- [70] N.L. Lanza, R.C. Wiens, R.E. Arvidson, B.C. Clark, W.W. Fischer, R. Gellert, J.P. Grotzinger, J.A. Hurowitz, S.M. McLennan, R.V. Morris, et al., Oxidation of manganese in an ancient aquifer, kimberley formation, gale crater, mars, Geophys. Res. Lett. 43 (14) (2016) 7398–7407.
- [71] W. Rapin, B. Bousquet, J. Lasue, P.-Y. Meslin, J.-L. Lacour, C. Fabre, R. Wiens, J. Frydenvang, E. Dehouck, S. Maurice, O. Gasnault, O. Forni, A. Cousin, Roughness effects on the hydrogen signal in laser-induced breakdown spectroscopy, Spectrochim. Acta Part B: At. Spectrosc. 137 (2017) 13–22, http://dx.doi.org/10.1016/j.sab.2017.09.003.
- [72] J. Manrique, J. San-Tamaría-Sancho, G. Lopez-Reyes, M. Veneranda, G. Arana, K. Castro, J. Madariaga, S. Maurice, C. Garcia, F. Rull, A. Sanz Arranz, R. Wiens, Evaluation Of similitudes Between Supercam And Simulcam, a laboratory Standoff Setup for Support science, in: 53rd Lunar and Planetary Science Conference, 2022, p. 2589.
- [73] J.A. Manrique-Martinez, G. Lopez-Reyes, A. Alvarez-Perez, T. Bozic, M. Veneranda, A. Sanz-Arranz, J. Saiz, J. Medina-Garcia, F. Rull-Perez, Evaluation of multivariate analyses and data fusion between Raman and laser-induced breakdown spectroscopy in binary mixtures and its potential for solar system exploration, J. Raman Spectrosc. 51 (9) (2020) 1702–1717, http://dx.doi.org/10.1002/jrs.5819.
- [74] K. Rammelkamp, S. Schröder, S. Kubitza, D.S. Vogt, S. Frohmann, P.B. Hansen, U. Böttger, F. Hanke, H.-W. Hübers, Low-level LIBS and Raman data fusion in the context of in situ mars exploration, J. Raman Spectrosc. 51 (9) (2020) 1682–1701, http://dx.doi.org/10.1002/jrs.5615.
- [75] S. Julve-Gonzalez, J.A. Manrique, M. Veneranda, I. Reyes-Rodríguez, E. Pascual-Sanchez, A. Sanz-Arranz, M. Konstantinidis, E.A. Lalla, M.E. Charro, E. Rodriguez-Gutiez, J.M. Lopez-Rodríguez, J.F. Sanz-Requena, J. Delgado-Igleais, M.A. Gonzalez, F. Rull, G. Lopez-Reyes, Machine learning methods applied to combined Raman and LIBS spectra: Implications for mineral discrimination in planetary missions, J. Raman Spectrosc. 54 (11) (2023) 1353–1366, http://dx.doi.org/10.1002/jrs.6611.

- [76] F. Rull, S. Maurice, I. Hutchinson, A. Moral, C. Perez, C. Diaz, M. Colombo, T. Belenguer, G. Lopez-Reyes, A. Sansano, O. Forni, Y. Parot, N. Striebig, S. Woodward, C. Howe, N. Tarcea, P. Rodriguez, L. Seoane, A. Santiago, J.A. Rodriguez-Prieto, J. Medina, P. Gallego, R. Canchal, P. Santamaría, G. Ramos, J.L. Vago, on behalf of the RLS Team, The Raman laser spectrometer for the ExoMars rover mission to mars, Astrobiology 17 (6–7) (2017) 627–654, http://dx.doi.org/10.1089/ast.2016.1567.
- [77] J.-P. Bibring, V. Hamm, C. Pilorget, J.L. Vago, the MicrOmega Team, The MicrOmega investigation onboard ExoMars, Astrobiology 17 (6–7) (2017) 621–626, http://dx.doi.org/10.1089/ast.2016.1642.
- [78] W. Rapin, S. Maurice, A. Ollila, R. Wiens, B. Dubois, T. Nelson, L. Bonhomme, Y. Parot, S. Clegg, R. Newell, L. Ott, B. Chide, V. Payre, C. Bedford, S. Connell, H. Manelski, S. Schröder, M. Buder, C. Yana, P. Bousquet, μ Libs: Developing a lightweight Elemental Micro-mapper For In Situ exploration, in: 55th Lunar and Planetary Science Conference, 2024, p. 2670.